The Thesis Committee for Lezli Giselle Matto González
Certifies that this is the approved version of the following Thesis:

Effect of Electrical Conductivity of pure and doped Lanthanum Chromite on the Onset of Selective Laser Flash Sintering

APPROVED BY
SUPERVISING COMMITTEE:

Desiderio Kovar, Supervisor

Joseph J Beaman

Effect of Electrical Conductivity of pure and doped Lanthanum Chromite on the Onset of Selective Laser Flash Sintering

by

Lezli Giselle Matto González

Thesis

Presented to the Faculty of the Graduate School of

The University of Texas at Austin

in Partial Fulfillment

of the Requirements

for the Degree of

Master of Science in Engineering

The University of Texas at Austin

May 2021

Dedication

To my family and my friends from Paraguay. You are always by my side.

Acknowledgements

To the Fulbright Scholarship, which provided me with funding to pursue my graduate studies here in the United States, and for making me part of a worldwide network of colleagues and friends who I know I can always count on.

To Dr. Kovar, for all the effort that you put into my graduate education. You guided me through courses and research, so I can become knowledgeable in my work, and ready for my career path. Your dedication and consistency are the reasons why I am able to graduate on time. Because of your support during my PhD applications, and also for your patience, I thank you.

To Dr. Beaman, for all your guidance and advice during my time working in the SLFS research group. Thank you.

Debbie, thank you for teaching me and training me in this research, for your knowledge, patience and all your help. You are the reason I was able to perform these experiments with confidence and you kept helping me even after you graduated. I can't thank you enough.

Alex, Andre and Nick, for being my friends and lab mates, for teaching me and helping me, and for sharing your everyday life with me during our time together at UT. I will always remember you.

Jeremiah, Derek, Doug and Stephen thank you for being there every time I needed help inside the laboratory. I can't tell you how much I appreciate you.

Krista, for your excellent work at TMI, and for all your kindness. You are outstanding and I appreciate you so much.

To my mentor Magna Monteiro and to Belén Martínez. Thank you for your words of encouragement, and for your support during my application for PhD programs. We finally made it.

Allie, thank you so much for all your help, your support, and words of encouragement. I have learned so much from you, and I hope to see you again soon.

To Yanina, Kaori, Camila, and all my Fulbright brothers and sisters. For sharing with me the Fulbright adventure during these unusual times that we are living.

To Maggie. You are so wonderful. You were there for me in so many unexpected situations during this past year, and your words of encouragement have helped me make it till the end, so thank you.

Yennifer, because you wake me up at 7:00 am when it is already 10:00 am in Paraguay. You kept me grounded during these whole two years away from home. I am so grateful for our friendship. I owe you everything. Thank you so much.

To my family: My Mother Rosaliz, my Father Rony, my sisters Sol and Janeth, my brother Rodrigo, and my niece Emma. For always being there for me, from the beginning until the end. I can't wait to see you again at home.

Finally, to all of you who directly or indirectly contributed to the completion of this work, and to whom have been there for me throughout these two years of graduate studies, I thank you.

Abstract

Effect of Electrical Conductivity of pure and doped Lanthanum Chromite on the Onset of Selective Laser Flash Sintering

Lezli Giselle Matto González, M.S.E.

The University of Texas at Austin, 2021

Supervisor: Desiderio Kovar

Selective laser flash sintering (SLFS) utilizes a large electric field applied during laser scanning to selectively partially sinter ceramics. This technique has previously been demonstrated in aluminum nitride and yttria-stabilized zirconia and is promising because it opens the possibility of binder-free additive manufacturing of ceramics. The purpose of this research is to study the effect of the electrical conductivity of ceramics on the initiation of SLFS. The materials chosen for this work were lanthanum chromite (LC), an intrinsic electronic conductor, and lanthanum strontium chromite (LSC), a ceramic that has even higher electronic conductivity due to doping. The results obtained show that for SLFS to initiate in these materials there is a critical applied electric field that is two order of magnitude smaller than for YSZ and AlN, and that a minimum laser power of only 3 W for LC and 4 W for LSC is required for SLFS to initiate. This is again significantly smaller than what has previously been observed for YSZ and AlN. The unexpected lower laser power needed to initiate SLFS in LC compared to LSC could be due to microstructural characteristics of the powders that influence their packing density and provide more

conductive paths in the pressed pellets. Studies of successive scans show that there is no significant history effect from previously parallel scanned lines on the current response of the successive lines which confirms that the effects of SLFS are localized to the near-scan regions. Varying scan directions also does not significantly affect the current measurement during SLFS in these materials. Results from partial scans that end on the negative electrode suggest that the charge carriers may follow the hot region under the scanning laser to the negative electrode, where the current measurement is obtained. Higher measured current for full scan lines compared to partial scan lines support the hypothesis that a combination of electrons produced at the positive electrode, temperature-activated intrinsic charge carriers, and extrinsic charge carriers present in LSC due to doping are the responsible for the relatively large current measured during SLFS of LSC even under modest laser powers and electric fields.

Table of Contents

List of Tables

List of Figures

Chapter 1: Literature Review

1.1. Solid Free-form Fabrication

Solid free-form fabrication (SFF) is a term used to describe processing technologies that allow the production of parts with the required geometrical complexity directly from a computer-aided design (CAD) without the use of traditional tools such as molds [1]. The value of SFF to the commercial sector is usually articulated in terms of reduced time to market (prototyping), low production "one-of-a-kind" parts and patterns for casting [2]. In contrast, the term Additive Manufacturing (AM) is used as a synonym for freeform fabrication [3].

1.2. Selective Laser Sintering

Selective laser sintering (SLS) is a type of additive manufacturing (AM) in which a high-powered laser fuses powdered materials without the need for part-specific tooling. The use of a computer-controlled, high-power laser to melt or sinter powder together is the basis for the system developed at the University of Texas and later commercialized by DTM Corporation [2]. A schematic of how the process works is shown in Figure 1.1. A thin layer of powder is spread over a base and a laser selectively scans the powder bed, sintering or melting the materials together. The bed is lowered slightly, a new layer of powder is spread over the selectively sintered layer, and the laser scans again, this time selectively sintering or melting powder together and into the preceding layer. This process is repeated until the desired part is completed.

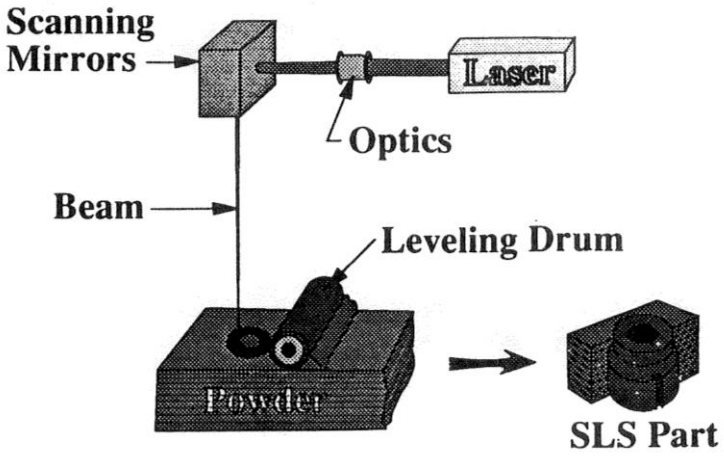

Figure 1.1. Schematic of the Selective laser Sintering Machine. Taken from Bourell (1990) [2].

For polymers and some metals, interaction of the laser beam with the powder raises the temperature to the point of melting, resulting in particle bonding and fusion of the particles to themselves as well as to the previous layer to form a solid object. Crystalline ceramics cannot be formed directly by SLS because of their very high melting temperatures and because matter transport by solid state diffusion is insignificant during short time of laser scanning. An indirect method for utilizing SLS to produce ceramics powder is to mix a polymeric binder mixed with the ceramic powder. The laser can then be used to melt the polymer, which provides the bonding phase for forming by SLS. Following binder removal, the body is sintered at high temperature to produce a dense object [1]. This indirect method for SLS is limited to small or thin-walled parts because binder removal without damaging the part is very challenging in thick-walled parts.

1.3. CONVENTIONAL SINTERING OF CERAMICS

Sintering is the process of transforming a powder into a solid body by heating to a temperature less than the melting temperature [4]. The powder is mixed with water or other materials (such as polymer and solvent) and formed to the desired shape by processes such as pressing, slip casting, extrusion, and injection molding. This "greenware" is then dried, any organic material removed, and the remaining particulate compact fired (sintered) at high temperature such that the particles bond together to form a solid polycrystalline (made of many small crystals or grains) ceramic [5].

As with all other irreversible processes, sintering is accompanied by lowering of the free energy of the system. The sources that give rise to this lowering of the free energy are commonly referred to as the *driving forces for sintering.* Three possible driving forces are:

1. the curvature of the particle surfaces
2. an externally applied pressure or field, and
3. a chemical reaction [1].

Figure 1.2 shows the stages of sintering in ceramics in which we start with a green part of packed powder (Figure 1.2. a)) which consists of 40-50% porosity. Figure 1.2. b) shows the initial stage of sintering where solid necks are formed with little or no densification. During the intermediate stage of sintering (Figure 1.2. c)), there is neck grow and the part begins to densify. Interconnected pores and grain boundaries are formed in this stage. Figure 1.2. d) shows the final stage of sintering where only isolated pores remain and the density continues to increase by shrinkage of the pores.

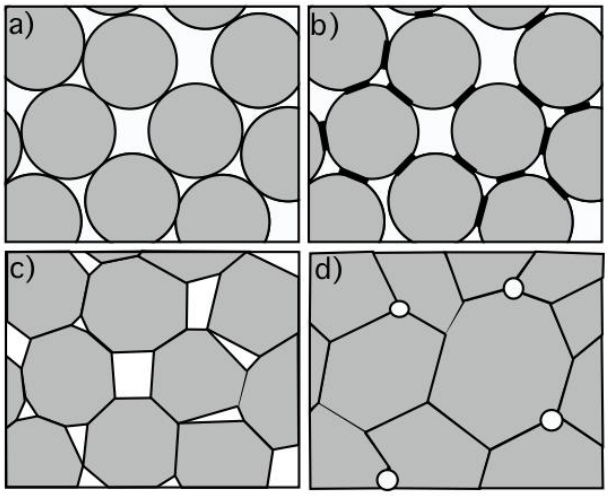

Figure 1.2. Sequence showing sintering process: a) Green part, consisting of 40-50% pores, b) Formation of necks between particles; volume fraction of porosity decreases slightly during the initial stages of sintering to about 35%, c) continuous pore channels and grain boundaries form during the intermediate stages of sintering; volume fraction of porosity decreases to about 10%, d) Final stage of sintering; pores are isolated and the rate of densification slows as the volume fraction of porosity approaches zero. Courtesy of Dr. Desiderio Kovar.

Mass transport during the sintering of polycrystalline ceramics occurs by diffusion, a thermally activated process, which can occur along several potential paths and by different mechanisms of diffusion: lattice, grain boundary, and surface diffusion [1]. Because of the large range in diffusivities, usually one mass transport path/mechanism is dominant at a given material and temperature.

The simplest model for sintering is that of two spheres in two dimensions shown in Figure 1.3. The source of mass to form the neck in Figure 1.3. a) is the surface of the particle, which does not result in densification. For densification to occur, the source of the mass must come from between the particle centers, as shown in Fig. 1.3 b) [4]. Table 1.1 lists diffusion paths and mechanisms and categorizes them by those that lead to densification and those that do not.

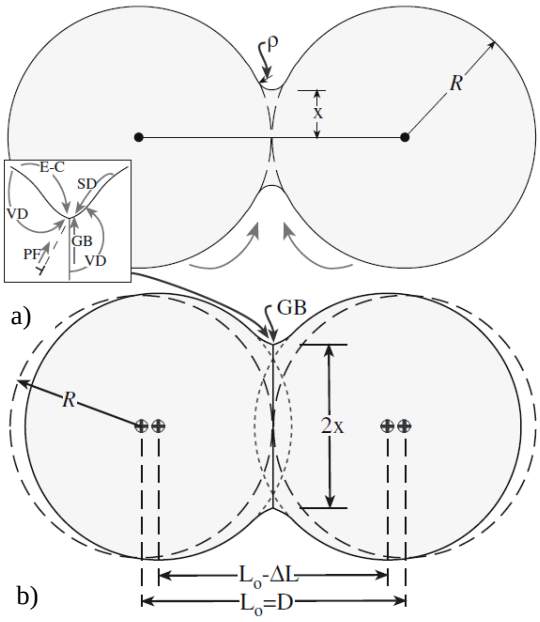

Figure 1.3. (a, b) Neck formation by mass transfer for a two-sphere model of radius R. a) a neck radius of x that has a radius of curvature ρ that is formed by surface diffusion of mass from the surfaces of the particles and b) shrinkage occurring by grain boundary diffusion from the particle boundary region to the neck. Taken from Barry Carter and Grant Norton (2007) [4].

Mechanism	**Source**	**Densifying**	**Non densifying**
Surface diffusion	Surface		x
Lattice diffusion	Surface		x
Vapor transport	Surface		x
Grain boundary diffusion	Grain boundary	x	
Lattice diffusion	Grain boundary	x	
Plastic flow	Dislocations	x	

Table 1.1. Mechanisms of sintering by mass transport to the neck [1].

Matter transport during sintering can be viewed in terms of the flux of atoms ions or, equivalently, in terms of the counterflow of vacancies. The flux of the diffusing species is driven by gradients in the concentration or in the more general case, by gradients in the chemical potential [1].

During pressureless sintering, the rate of atomic (or ionic) rate of diffusion depends on the temperature and the concentration of defects in the solid. The defect concentration can be varied by changing the temperature, the oxygen partial pressure (or atmosphere), and the concentration of dopants or impurities [1]. Additional driving forces that influence the rate of diffusion include the application of a pressure, or when the diffusing species are charged, an electric field.

1.4. FLASH SINTERING

Flash sintering was first introduced by Cologna *et al.* in 2010 [7]. This method is adapted from conventional furnace-based sintering: the difference is that an electric field is applied by means of two platinum electrodes to a dog bone shaped sample as shown in the Figure 1.4. The electrode wires also serve the purpose of suspending the specimen into the hot-zone of the furnace [8].

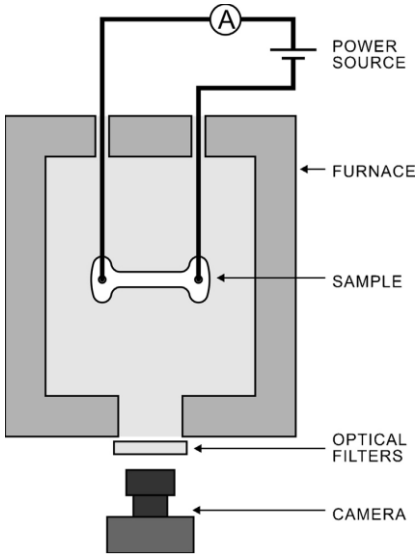

Figure 1.4. Schematic of the flash sintering experiment. Taken from Yoshida *et al.* (2014) [7].

Cologna *et al*. showed that 3YSZ can be sintered in a few seconds at approximately 850ºC to full density starting from a 50% green density by the application of a DC electric field. A process that would normally take several hours in a furnace at 1450ºC [6].

The phenomenon of flash-sintering is characterized by two experimental observations:

1- at a certain temperature and applied electrical field there is a sudden increase in the sintering rate such that sintering occurs in just a few seconds. A higher applied field lowers the temperature for the onset of flash-sintering.

2- The sintering event is accompanied by a sharp increase in the conductivity of the ceramic, which occurs at the same temperature and applied field [8].

Flash sintering can be separated in three stages [9]. These stages are based primarily on the measured current density through the sample and the densification of the sample [10]. During Stage I, an abrupt increase in conductivity, after an incubation time is

observed. In Stage II there is rapid densification and a sharp increase in electric current flowing through the sample. The continuous rise in conductivity can lead to thermal runaway under voltage control, therefore the power supply is switched to current control when a critical current is reached. The sample can reside indefinitely under current control which is called Stage III of flash sintering [11].

Figure 1.5 shows a characteristic current and densification versus time curve for flash sintering. Time is plotted on the horizontal axis and current (orange curve) and shrinkage (green curve) are plotted on dual vertical axes [10].

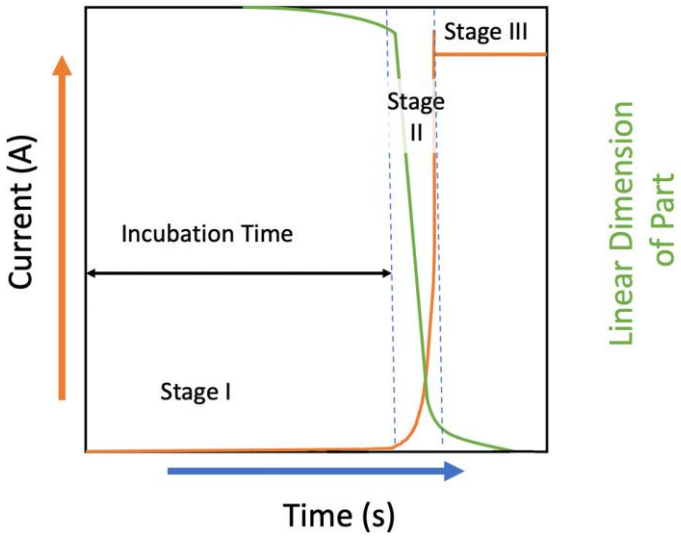

Figure 1.5. Stages of flash sintering. Taken from Hagen *et al.* (2020) [10].

Some of the materials that have been study with this technique include: 3YSZ [12][13][9], 8YSZ[14][15][16], MgO-doped alumina [8], Co_2MnO_4 [17], $BaTiO_3$ [18], $La_{0.6}Sr_{0.4}CoFe_{0.8}O_3$ [19], Y_2O_3 [7] and $MgAl_2O_4$ [20], among others.

1.5. Mechanisms for Flash Sintering

Even though several intrinsic and extrinsic factors related to flash sintering have been explored the description of the mechanisms behind the actual sintering process remains a challenge [21].

Several proposed mechanisms for the flash sintering phenomenon have been suggested: The retardation of grain growth through the influence of the electric field on the space charge in the grain boundaries [12], increase of the sample temperature by joule heating [22], the creation and migration of Frenkel pairs [13], and localized heating at the grain boundary[14].

Joule heating is considered to be the primary effect of the primary current pulses through the specimen, leading to temperature increase at the intergranular region, with consequent decrease of the electrical resistance, increase in the mobility of charge carriers (mainly oxide ions) increase in the intergranular defect diffusion and final densification in a relative short time, inhibiting grain growth [21].

1.6. Selective Laser Flash Sintering of Ceramics

In 2018 Hagen *et al.*[23] proposed a new direct selective laser sintering technique that combines laser heating with an electric field to partially sinter ceramic powders, which they named Selective Laser Flash Sintering (SLFS). In this approach a laser is used in conjunction with an electric field to induce initial stage sintering of the part to a sufficient degree that necks are produced between the particles such that the part will hold together wherever the laser was scanned over the powder bed. This process is repeated one layer at a time until a bulk part is fabricated. Final densification is accomplished in a post-processing firing [24]. Materials that have been studied with this technique include 8YSZ [25] [26] [24] and AlN [27].

1.7. ELECTRICAL CONDUCTIVITY OF CERAMICS

Ceramics show the widest range of electrical properties of any class of materials. At one extreme we have high-temperature superconductors, which have no resistance to an electrical current. At the other extreme we have electrical insulators. The conduction mechanisms in ceramics can be quite complex and may involve the movement of electrons, holes, and ions: in some case they may be "mixed", with more than one type of charge carrier responsible for current flow [4].

In comparing values of conductivity (σ) and resistivity (ρ) it is useful to remember the simple relationship between them:

$$\sigma = \frac{1}{\rho} \qquad 1.1$$

Electrical conductivity is given by:

$$\sigma = n \cdot q \cdot \mu \qquad 1.2$$

where n = the number of charge carriers that have mobility = μ and charge = q.

The importance of this equation is that it applies to all materials. If more than one type of charge carrier is contributing to σ then we can define a partial conductivity for each. For example, if σ were due to the movement of electrons and cations with a charge Z, then for electrons

$$\sigma_e = n_e \cdot q \cdot \mu \qquad 1.3$$

and for cations:

$$\sigma_+ = n_+ (Z \cdot \mu) \qquad 1.4$$

where n_e = the number of electrons and n_+= the number of cations of valence Z.

The total conductivity would be:[4]

$$\sigma_{tot} = \sigma_e + \sigma_+ \qquad 1.5$$

1.8. LANTHANUM CHROMITE AND STRONTIUM-DOPED LANTHANUM CHROMITE

$LaCrO_3$ was developed in the 1960s for electrodes in magnetohydrodynamic (MHD) generators where the electrodes had to withstand temperatures up to 2000ºC and the corrosive potassium atmosphere in the generator. MHD are now of little interest, but $LaCrO_3$ has received renewed interest for electrodes in solid oxide fuel cells (SOFCs) because of its unusually high electrical conductivity (for a ceramic), even at modest temperatures[4]. The electrical conduction in $LaCrO_3$ is almost wholly electronic[28].

The interconnects for SOFC must separate fuel and oxidant gases and also have high electronic conductivity at high temperature (773 – 1273K). Therefore, interconnects should meet the following requirements:

1. High density so that gas cannot permeate through the electrode
2. High electronic conductivity without oxygen electrochemical leak
3. Chemical stability in both oxidant and fuel atmospheres
4. Thermochemical compatibility with the other cell components

To meet the further increase the conductivity and improve sinterability, the composition of $LaCrO_3$ was modified by doping of lower valence alkaline ions, such as Ca^{2+}, Mg^{2+}, and Sr^{2+}, at the La^{3+} or Cr^{3+} sites [29].

Doped $LaCrO_3$ is a p-type conductor, and the electronic conductivity increases with concentration of low-valence cations, such as Sr^{2+} or Ca^{2+} in La^{3+} [29]. The introduction of divalent impurities gives lanthanum chromite a carrier concentration and conductivity much greater than for pure material [28].

In 1969, Meadowcroft reported that Sr-doped $LaCrO_3$ with the composition of $La_{0.84}Sr_{0.16}CrO_3$ exhibited a thermal conductivity of 5.1 W/m·K between 1100 K and 2000 K. In his work he also studied the temperature dependance of the electrical conductivity of

doped and undoped lanthanum chromite and the plots of their results are reproduced in Figure 1.6 a) and b).

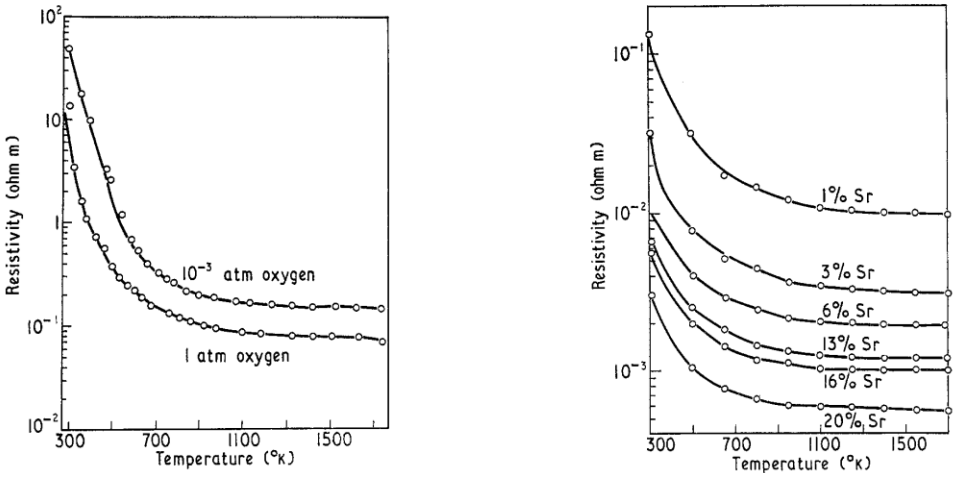

Figure 1.6. The temperature dependance of the electrical resistivity for a) undoped lanthanum chromite and b) for a series of samples of Sr-doped lanthanum chromite ($La_{1-x}Sr_xCrO_3$). Taken from Meadowcroft (1969) [28].

In their work they found a linear relationship between log(ρ/T) and 1/T from room temperature up to 1800 K. Linearity over such a wide temperature range is good evidence for validity of the equation:

$$\rho \propto T \exp\left(\frac{E}{kT}\right) \qquad 1.6$$

where E = the activation energy for conduction.

It is seen that the behavior of doped lanthanum chromite differs from that of the undoped materials. Whereas in the latter a collective electron model seems appropriate, the results on heavily doped materials suggests a localized model [28]. Meadowcroft's data show low activation energy at high temperature. This data suggests that it is reasonable to assume that all the positive holes induced by doping with strontium are free at the higher temperatures so that the activation energy at high temperatures is only associated with the

hole mobility. Therefore, the absence of a change in activation energy signifies that the carrier density is constant down to room temperature, and that the change in conductivity must be entirely due to a varying mobility, which implies that electrons are localized [28].

The conductivity of doped lanthanum chromite is approximately proportional to the strontium content; if there is no compensation, then the carrier density must be equal to the strontium content at all measured temperatures. With this assumption the mobility can be deduced to be approximately 5×10^{-7} $m^2V^{-1}s^{-1}$ at 300 K and approximately 3×10^{-6} $m^2V^{-1}s^{-1}$ at 1400 K with an activation energy for mobility falling from 0.13 to 0.10 eV with increasing strontium content.

Chapter 2: Experimental Procedures

The powders used for this work were lanthanum chromite and lanthanum strontium chromite, purchased from American Elements® (Los Angeles, CA) both of 99% purity. The chemical formulas and product code for each powder is provided in Table 2.1. No additional details of the powders were provided by the manufacturer.

Name	Chemical formula	Product code
Lanthanum chromite	$LaCrO_3$	LA-CRIT-02R-P
Lanthanum strontium chromite	$La_{0.8}Sr_{0.2}CrO_3$	LASR-CRIT-02R-P.20SR

Table 2.1. Product information of powders used in this work.

2.1. X-RAY DIFFRACTION (XRD)

X ray diffraction was performed on the purchased powders using a Rigaku Miniflex 600 with Cu Kα radiation. The goal was to determine the phase purity of the powder since powder processing routes for making these materials may produce powders that are not fully reacted from their precursors or they may contain impurities. These undesirable phases are known to affect the properties of these materials. The experiments were conducted using a θ - 2θ configuration with an accelerating voltage of 40 kV and a current of 15 mA in a continuous scan mode at a scan speed of 1.5 deg/min. The powder samples were scanned from 2θ = 20° to 80° and the resulting diffraction peaks were compared to the known peaks for $LaCrO_3$ (PDF # 01-074-1961) and $La_{0.8}Sr_{0.2}CrO_3$ (PDF # 01-074-1980) using the International Centre for Diffraction Database (ICDD) database.

2.2. PELLET PREPARATION

Pellets were prepared by uniaxial pressing the powders without additives using a carbide die and hardened steel punches. Prior to pressing, the die and punches were lubricated with a 2% solution of steric acid in acetone to reduce friction. The lubricant was applied to the punches and die using a cotton swab. The acetone was allowed to evaporate, leaving a thin layer of steric acid on the die and punch surfaces. After inserting the bottom punch and introducing a measured amount of powder into the die, the top punch was inserted and a manual hydraulic press (Carver®, Model #3912, Wabash, IN) was used to press the pellets into cylindrical pellets at a pressure of 5000 psi. The final pressed pellets had a diameter of 25.4 mm and a thickness that varied from 3.10 to 3.60 mm. After pressing the pellets, their surfaces were wiped to remove any residue left from the lubricant or from erosion products from the die.

Electrodes were manually painted on opposite sides of the pellets with colloidal silver paint (Pelco® silver paint, Ted Pella, Redding CA). The gap between the electrodes (i.e., the region on the pellet surface that consisted of bare ceramic) was measured on two sides of the pellet, and then averaged. The pellets were then heated in an oven at 125 ºC for 1 to 2 hours to remove any moisture present on the powder surfaces. Pictures of two representative pellets made for these experiments are shown in Figures 2.1a and 2.1b.

a)

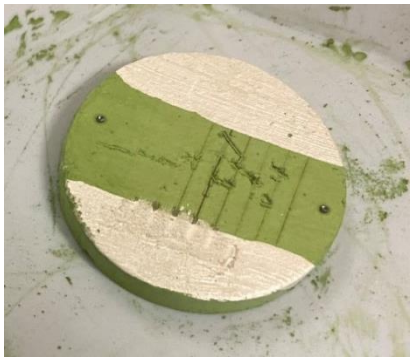

b)

Figure 2.1. Pictures of representative samples showing the electrodes (white) and bare pellet surfaces (brown or green) of a) lanthanum strontium chromite pellet and, b) lanthanum chromite pellet.

2.3. SELECTIVE LASER FLASH SINTERING (SLFS)

The SLFS machine was custom-built and is shown schematically in Figure 2.2a. The only external heat source was a focused continuous wave CO_2 laser (Model 48-5, Synrad, Mukilteo, WA) with a wavelength of 10.6 μm and maximum power of 55 W. The beam was focused with ZnSe optics (Edmund Optics, Barrington, NJ) and scanned on the surface of the sample with a set of ZnSe mirrors connected to a pair of galvanometers (6240H, Cambridge Technology, Bedford, MA). The beam profile was measured using a beam profiler (NanoScan v2^{TM}, Ophir, Jerusalem, Israel) and was determined to be pseudo-Gaussian with a full width at half maximum of 380 μm. Parameters that were varied for this work were laser power (LP) and the voltage applied to the electrodes of the sample. The applied electric field (EF) was calculated by dividing the voltage by the gap distance between the electrodes. All the experiments for this work were performed at a laser scan speed of 100 mm/s. The laser power was varied from 3 to 8 W (0.03 – 0.08 J/mm) and the electric field was varied from 15 to 41 V/cm. The resulting scanning laser energy density was calculated from:

$$Laser\ Energy\ Density = \frac{(Laser\ power, W)}{(Scan\ Speed, mm/s)(Beam\ Area, mm^2)} \quad 2.1$$

and varied from 0.26 – 0.70 J/mm^3.

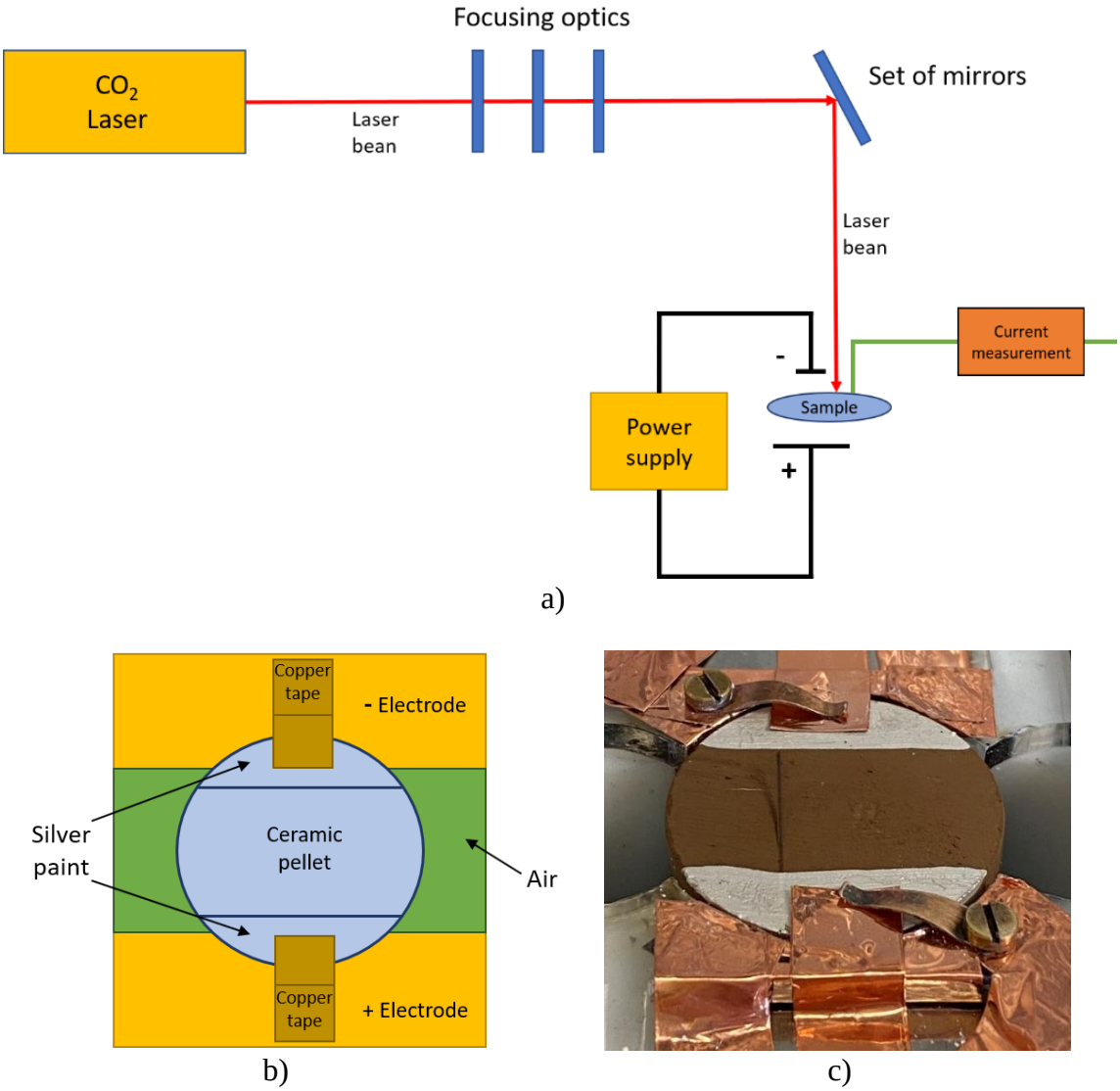

Figure 2.2. a) Schematic representation of the SLFS machine, b) Plan view showing details of the sample set up, and c) Picture of the experimental set up of the sample for the SLFS experiments.

The pellets were placed in the sample holder of the SLFS machine and then attached to the positive and negative stainless steel electrodes (shown in yellow) with copper tape (Ted Pella) as shown in figure 2.2a and b. The stainless steel electrodes were separated by air as shown in green in Figure 2.2c. A voltage ranging from 20 to 50 V was applied to the pellet with a DC power supply (PS350, Stanford Research Systems, Inc., Sunnyvale, CA) to generate the electric field. All the experiments for this work were performed in air atmosphere.

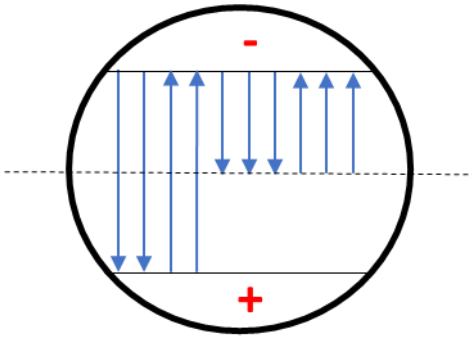

Figure 2.3. Representative diagram of scanned lines and directions for the set of experiments conducted in this work.

The laser was control through the software ScanMaster^{TM} Designer (version 3.0.20) with which it was possible to set the parameter for each scanned line. Parameters such as laser power, laser scan speed, position of the lines, and scan direction were controlled with this software.

10 equally distributed lines were scanned per each pellet. Studies of the effect of laser scan direction and partial scans were also performed in this work as illustrated in Figure 2.3. Full scanned lines were performed from the positive to negative electrode, and from the negative to positive electrode, and the current was measured and recorded

throughout the experiment at a frequency of 500 Hz using an integrated data acquisition and control system (Compact RIO 9035, National Instruments, Austin TX) with a current measurement module (NI-9207, National Instruments, Austin TX). Partial scans were also performed on the pellet surface starting from the negative electrode and finishing near the middle of the pellet and starting near the middle of the pellet and finishing on the negative electrode. The full scan lines were 17 mm length, and the partial scan lines were of 8.5 mm length. All the lines were equally distributed with a 2 mm average distance between one another. The voltage signal was recorded simultaneously with a voltage measurement module (NI-9201, National Instruments, Austin TX) to correlate the current measurements and the laser on/off times.

2.4. SCANNING ELECTRON MICROSCOPY (SEM)

Scanning electron microscopy (SEM) was performed on the as-received powder and on the pellets using an SEM equipped with a field-emission electron source (Quanta 650, FEI, Hillsboro, OR) to study particle size, particle shape, and the degree of sintering of the powders. Plan view images were obtained from the regions scanned by the laser and away from these regions to compare neck formation in each region. This technique was also used to verify if cracks were formed on the scanned lines.

For powder preparation, they were suspended in ethanol and drops of the suspensions were places on the SEM stubs and allowed to dry before placing them on the SEM chamber for analysis.

The pellets where mounted on SEM stubs with conductive carbon glue (PELCO®, Ted Pella, Redding, CA), allowed to evaporate for 5 minutes and cure for an additional 24 hours before placing the samples in the SEM. Because of the relatively high electrical conductivity of these materials, coating of these samples using sputtered gold as is typically done with ceramic samples was not necessary.

Chapter 3: Results and Discussions

3.1. Powder Characterization

Results from XRD analysis of the powders used to prepare specimens are shown in Figure 3.1. The characteristic diffraction peaks for lanthanum chromite and the lanthanum strontium chromite were compared to the theoretical peak locations from PDF 01-074-1961[30] and PDF 01-074-1980 [30], respectively. Peaks positions for both compounds are very close to each other but the peaks for the strontium-doped lanthanum chromite (LSC) are shifted slightly to the right relative to the undoped material (LC). In both cases the experimentally measured diffraction peaks are a good match to the locations and intensities of theoretical peaks. However, the doped powder exhibits a few very small additional peaks at 2θ = 22.9˚1 and 2θ = 32.65˚ that may be from precursors that did not fully react during synthesis.

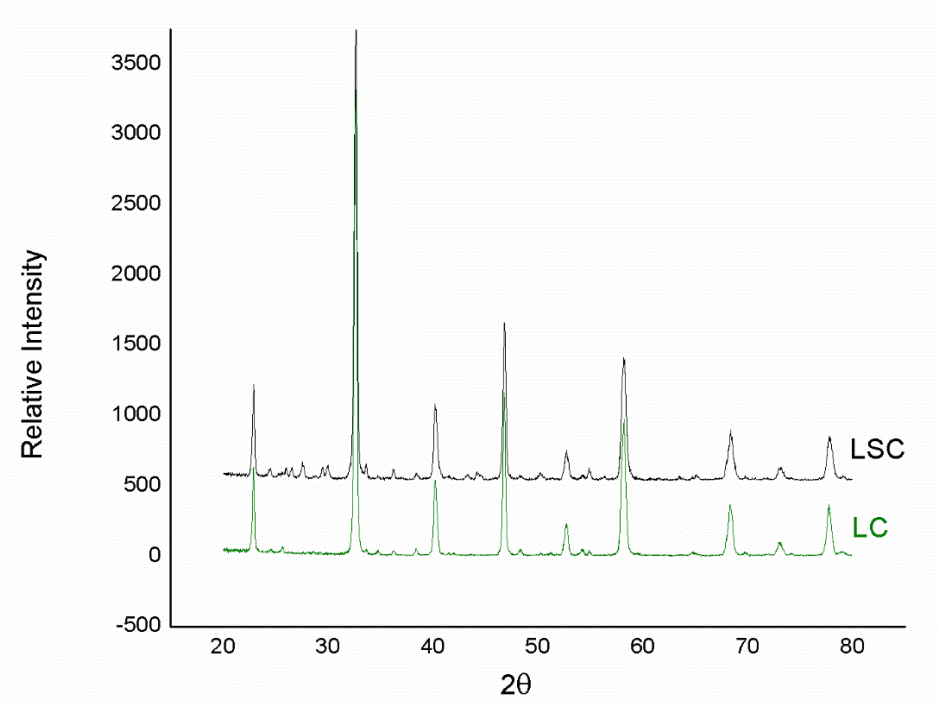

Figure 3.1. X-Ray diffractograms of the as-received powders for 20° < 2θ < 80°.

Representative scanning electron microscopy (SEM) images of the as-received powders are shown in Figure 3.2 a) and b). From these images it is apparent that the doped lanthanum strontium chromite powder exhibits larger agglomerates than the undoped lanthanum chromite powder. This is significant because agglomerated powders tend to result in parts with lower green densities when the powders are pressed into pellets. The lower green densities are expected to result in fewer conductive paths in the pressed pellets. On the other hand, the LSC powder show slightly larger primary particle size.

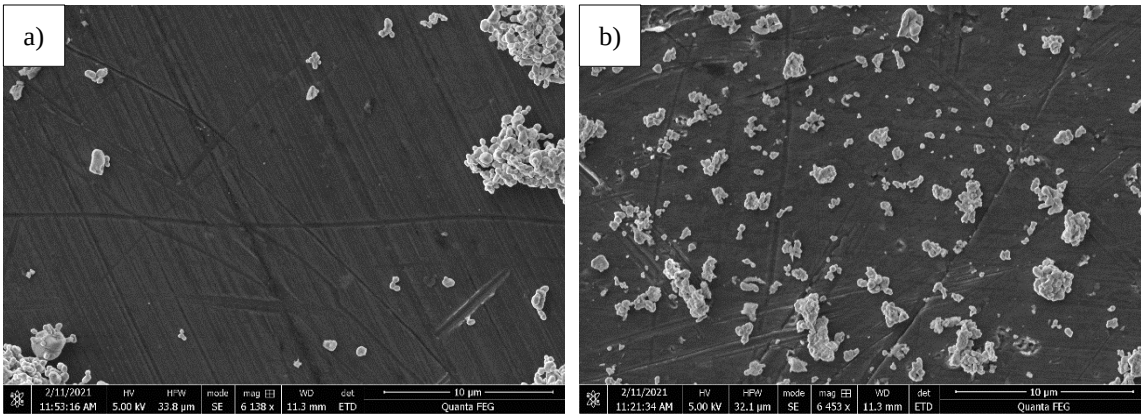

Figure 3.2. SEM images of the as received powders a) lanthanum strontium chromite and b) lanthanum chromite.

3.2. PELLETS CHARACTERIZATION

An average value of the green density of the samples used for this work are shown in Table 3.1, which shows a slightly higher green density for the LC than for the LSC which is consistent with the smaller agglomerates of particles seen in LC than LSC in the SEM images from section 3.1.

Sample	Average green density
LSC	3.04 g/cm^3
LC	3.08 g/cm^3

Table 3.1. Average values of the green density of samples used for this work.

Representative images of the pellets surfaces after pressing are shown in Figure 3.3. The bare pressed powder at the sample's surface of LSC shows again larger agglomerates than the LC sample.

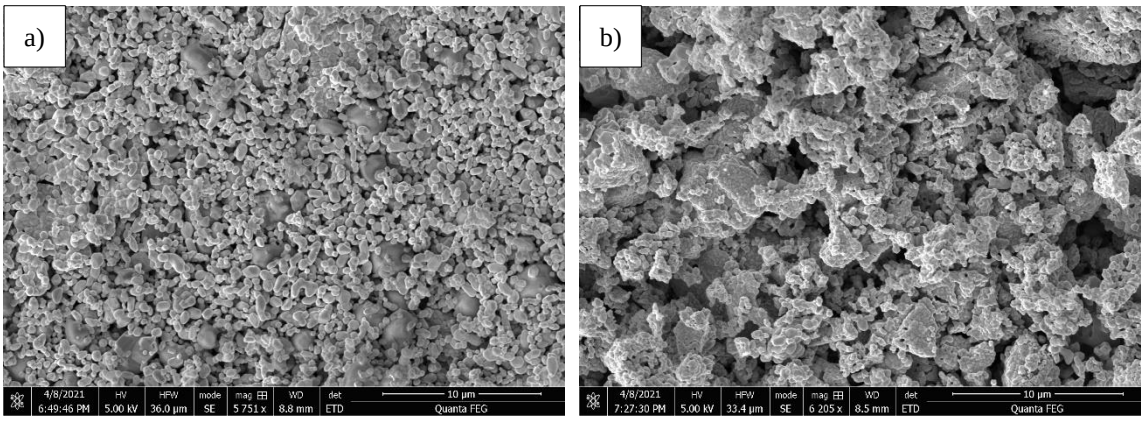

Figure 3.3. SEM images of the a) LSC pellet surface and b) LC pellet surface.

3.4. STUDY OF APPLIED ELECTRIC FIELD ON THE ONSET OF SLFS FOR LSC AND LC

Studies of the influence of applied electric field on the initiation of SLFS on LSC and LC were performed with and without an applied electric field to the samples and results are shown in Figures 3.4 a) – d). The laser scan pattern used for these experiments is shown in Figure 3.4 e).

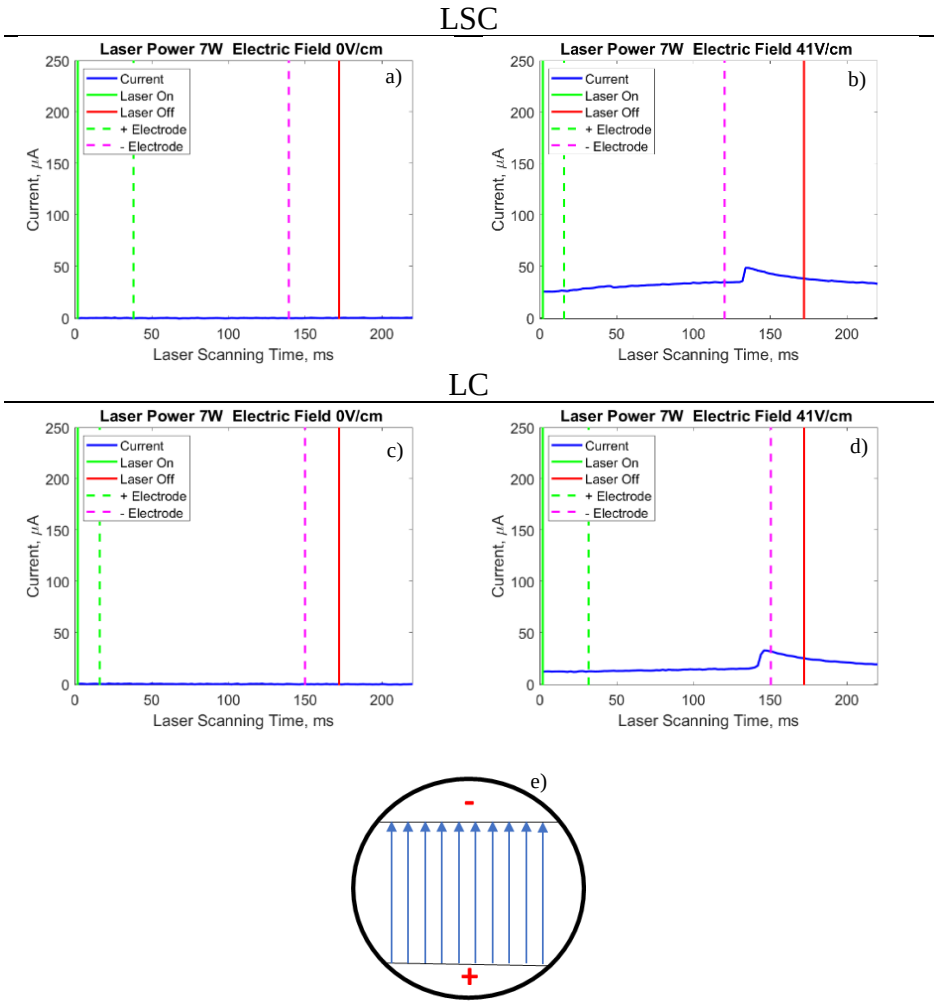

Figure 3.4. Influence of electric field on the initiation of SLFS of LSC for an applied electric field of a) 0 V/cm and b) 41 V/cm, and of LC for an applied electric field of c) 0 V/cm and d) 41V/cm. These experiments were performed at a laser power of 7 W and laser scan speed of 100 mm/s.

Ten parallel lines were scanned successively at a laser power of 7 W were scanned to a sample of LSC with no applied electric field. For each scan, no current rise was detected. A representative current measurement for a scanned line is presented in Figure 3.4 a). Another experiment was conducted on a nominally identical sample, but in this case an applied electric field of 41 V/cm was applied. A representative current measurement during scanning of a line at a laser power of 7 W and a scan speed of 100 mm/s is presented in Figure 3.4 b). This measurement shows a starting leakage current of about 25 μA. This indicates that under an applied DC electric field of 41 V/cm, the LSC is electrically conducting even at room temperature. When the scan commences, there is a slow rise in current as the laser beam leaves the positive electrode and travels across the pellet surface towards the negative electrode. A current spike of about 50 μA is visible when the laser beam approaches the negative electrode at a time of approximately 150 ms. The peak has been attributed to the initiation of SLFS. After the peak in current, it decays more slowly to about the value of the original leakage current. Note that the positions of the positive and negative electrodes were measured manually with calipers so there is some uncertainty in those measurement. However, the laser on/off lines exhibit much less uncertainty since those signals are obtained digitally from the software that controls the laser.

The same experiments were performed on LC samples and the current measurements are shown in Figure 3.4 c) and d). A representative current measurement for the experiment conducted with 0 V/cm of electric field is shown in Figure 3.4 c) and again, no current rise was measured. For the experiment with an applied electric field of 41 V/cm (Figure 3.4 d)) a leakage current of about 15 μA was measured prior to commencing the scan. This leakage current for the undoped LC is about 40% lower than what was measured for the doped LSC powder. The smaller leakage current is expected because of the much lower intrinsic electrical conductivity of LC versus LSC. In fact, it is somewhat surprising

that the differences in leakage current are not more substantial given that LC exhibits an intrinsic conductivity three orders of magnitude lower at room temperature, and two orders of magnitude lower at temperatures above 1100 K compared to LSC [28]. The relatively small difference in leakage current could be because the lower intrinsic conductivity could be offset by the higher green density of the LC pellets compared to LSC.

As was observed for LSC, as the scan commences, there is a slow rise in current as the laser beam leaves the positive electrode and travels across the pellet surface towards the negative electrode and a current spike is visible when the laser beam approaches the negative electrode at a time of approximately 150 ms. Compared to LSC, the current spike of about 40 μA was about 20% lower for LC. Finally, the current decays slowly to a value of about the original leakage current.

From these experiments it is apparent that when no field is applied to the samples, there is no leakage current. The current remains near zero throughout the experiment when the laser is turned on and scans the sample from the positive to the negative electrode. This occurs for both LSC and LC powders and confirms that SLFS is not initiated in this material system without an applied current.

When a sufficiently large electric field (in this case 41V/cm) is applied to the samples a leakage current is detected in both samples, but the current is larger for LSC than for LC. This is consistent with the known higher intrinsic electrical conductivity for LSC compared to LC.

Comparing the measurements of Figure 3.4 b) and d), it is apparent that the gradual current rise that occurs as the laser leaves the positive electrode and scans across the pellet surface is greater for the LSC than for LC. For example, the current increase before the spike is observed for LSC is about 12 μA whereas for the LC the current increases by less than 6 μA. The current rise during scanning must be associated with an increase in the

effective carrier concentration or mobility, but further experiments discussed below are needed to clarify the source of this increase.

Both samples exhibited a current spike with an applied electric field of 41 V/cm, a laser power of 7 W and 100 mm/s scan speed. This behavior is qualitatively similar to what have been seen before for AlN and YSZ [26] [31] ; a current spike occurs only when a critical combination of laser power and electric field is applied to the samples and when the laser reaches the negative electrode. However, the combinations of electric fields and laser powers required to initiate a current spike was much larger for both AlN and YSZ. For example, for YSZ a field of 1500 V/cm and a laser power of 8.5 W was required to initiate a current spike. Thus, the initiation of SLFS in LSC and LC is considerably easier compared to previously tested ceramics.

3.5. EFFECT OF LASER POWER ON THE ONSET OF SLFS FOR LSC AND LC

Studies of the effect of laser power on the onset of SLFS were performed on LSC and LC samples using the same scan pattern shown in Figure 3.4 e), and the current measurements graphs are shown in Figure 3.5. and Figure 3.7.

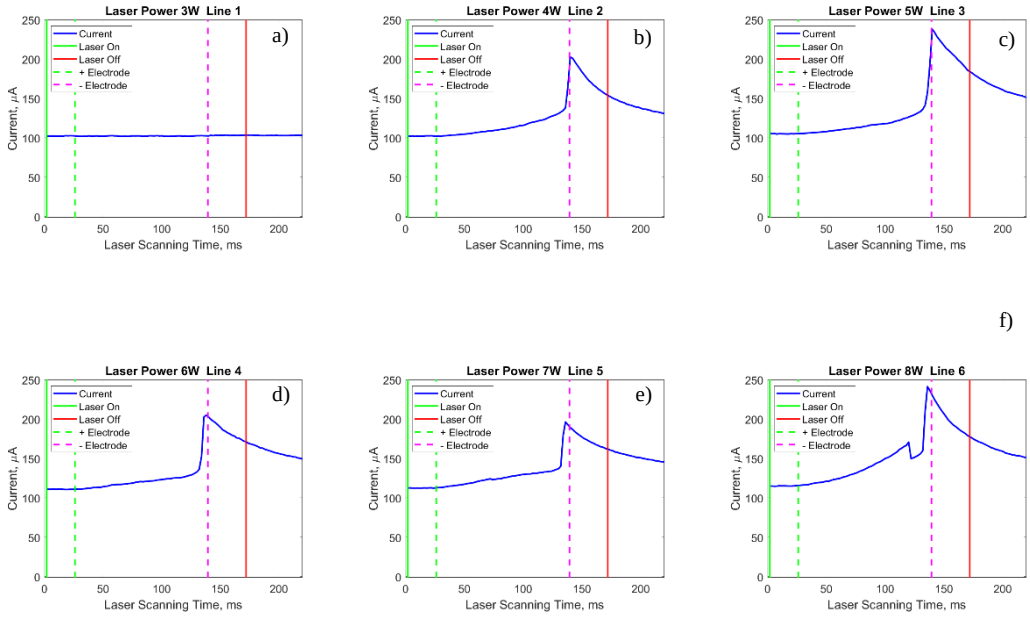

Figure 3.5. Influence of laser power on onset of SLFS in LSC for a laser scan speed of 100 mm/s, applied electric field of 41 V/cm and laser power equal to a) 3W, b) 4W, c) 5W, d) 6W, e) 7W, and f) 8W.

An initial leakage current of about 110 μA is observed on this sample prior to the first scan. Note that this leakage current is significantly larger than shown in Fig. 3.4 for the same material tested at the same applied field. This difference in leakage current could result from pellet-to-pellet variations in particle packing density or defect density that arise during pressing of the pellets, either of which would affect the measured leakage current because they would change the effective conductivity. This variability could also be due to the differences in the thickness or properties of the electrodes that were made from silver

paint, or from differences in the contact resistance between the samples and the copper tape that connected the painted electrodes to the stainless steel electrodes used in the specimen supports. Considering all specimens of LSC that were tested, the leakage current for an applied electric field of 41 V/cm was observed to vary from 25-110 μA from pellet to pellet.

At a laser power of 3 W (Fig. 3.5a)), there is no significant increase in measured current observed during the scan. When the laser power is increased to 4 W (Fig. 3.5b), the current gradually begins to increase as the laser scans across the pellet surface until a spike in current of approximately 75 μA is observed as the laser approaches the negative electrode. Increasing the laser power to 5 W for the next line results in similar increases in current during laser scanning across the pellet surface, but an even larger current spike of over 100 μA when the laser reaches the negative electrode. Further increases in laser power to 6 W results again in similar increases in current during scanning across the pellet surface, but the current spike upon reaching the negative electrode is reduced to approximately 85 μA and increasing the laser power to 7 W results in a further reduction in the current spike to less than 75 μA. Line 6 at a laser power of 8 W exhibits a large increase in current as the laser scans across the pellet surface but there is a sharp drop in current before the current spikes by approximately 100 μA. The cause of the drop in current is not known but it could be due the initiation of a large crack in the pellet during laser scanning.

Tests on other LSC samples (data presented in Section 3.6) showed that samples with higher leakage current were observed initiate SLFS at lower laser power and the magnitude of the current spikes were observed to be larger than for samples that had lower observed leakage current. This suggests that highly conductive paths result in onset of SLFS at lower laser powers.

In summary, these results show that, similar to other materials that have been tested, there is a critical laser power to initiate SLFS for a given E-field and scan speed. For this material we were also able to show that there is an influence of the leakage current on the initiation of SLFS. For the conditions shown in this experiment with an applied electric field of 41 V/cm, 100 mm/s scan speed and about 110 µA of leakage current, the initiation of flashing was observed at a laser power of 4 W. These values of laser power and electric field are dramatically lower than what has been observed for other materials[26] [31], which confirms that SLFS is far easier to initiate in LSC compared to AlN or YSZ.

SEM imaging of the samples in the vicinity of the scanned lines was performed to observe changes in the powder morphology and sample integrity where scanning had occurred. SEM images of lines 2, 3, 4 and 5 are shown in Figure 3.6. A region of brighter contrast is visible in the SEM images where the laser scanned suggesting that the powder morphology was altered by the laser. In addition, channel cracks are visible running perpendicular the scanning direction and sample surface. Previous experiments conducted on YSZ show similar cracks can form and the severity of the cracking was observed to increase when the current spikes were larger, suggesting that the cracks result from thermal shock [10]. Imaging performed with a high-speed camera on YSZ suggest that the cracking occurs following passage of the laser upon cooling of the partially sintered sample, rather than upon heating [32]. The distance behind the laser where cracking was observed can be up to several beam diameters. When smaller laser powers were employed with YSZ such that the magnitude of the current spikes was limited to less than 20 µA, the incidence of cracking reduced significantly, suggesting that it may be possible to avoid cracking if the peak currents are reduced sufficiently. It is notable that all of the lines in Fig. 3.6 exhibited channel cracks, but none of the scan conditions produced peak currents less than 20 µA so

it is possible that better control of the laser scan conditions to minimize the magnitude of the current spikes could be used as a strategy to reduce cracking.

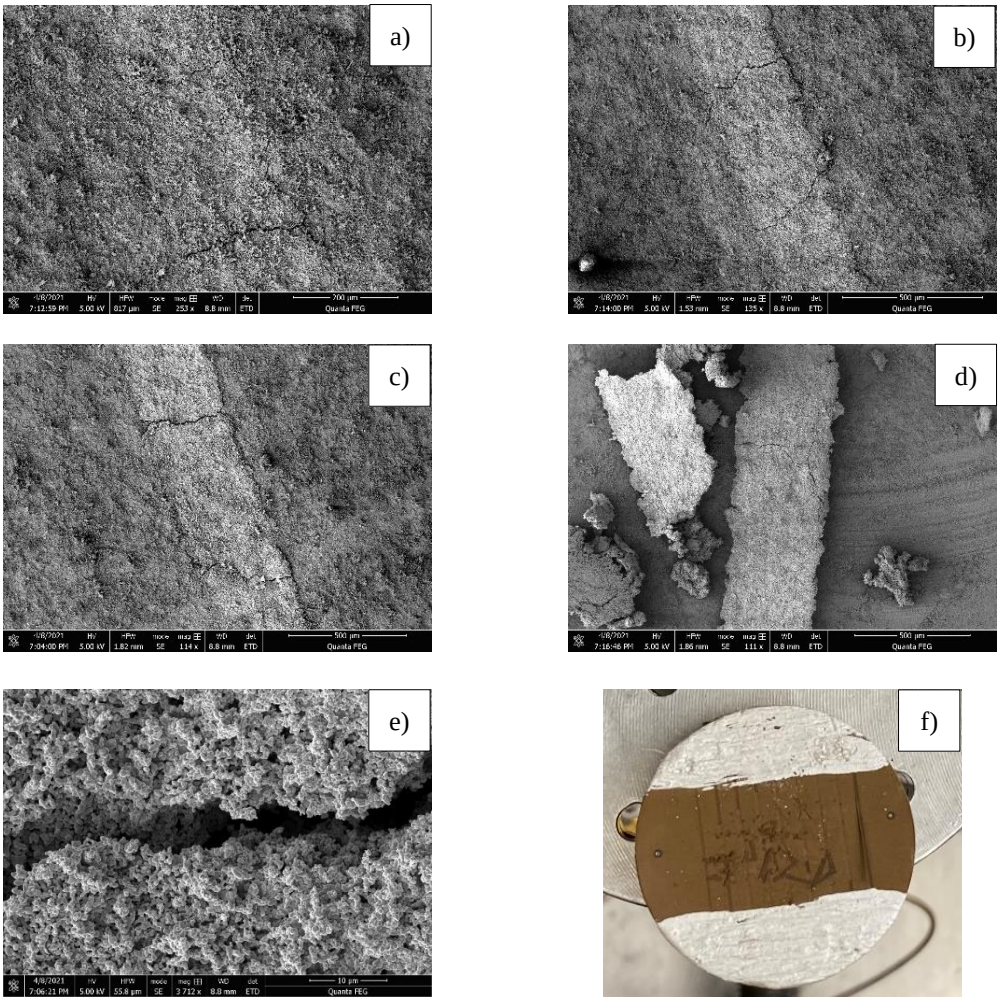

Figure 3.6. SEM images showing evidence of partial sintering and cracking in a) line 2 at a laser power of 4 W, b) line 3 at a laser power of 5 W, c) line 4 at laser power of 6 W and d) line 5 at laser power of 7 W. A magnified view of a channel crack in line 4 is shown in e). f) Shows a picture of the pellet used in this study. After the first 6 lines in this pellet were scanned, they were cut with a razer blade and subsequent experiments which are explained in the next sections were ran in this same pellet.

The presence of cracks could influence the current behavior during SLFS because they impede current flow along the length of the scanned line. Cracks that initiate later in the process or have a shallower depth may have minimal impact on the current response during SLFS if there are still conducting paths available for current flow, but more severe cracks that penetrate deeper in the sample or cracks that initiate within the laser spot would be expected to more strongly influence the current behavior. The increased severity of channel cracks with laser power may explain the non-monotonic response of the lines to increasing laser power shown in Figure 3.5. The expected monotonic increase in the current spike with laser power that has been observed in AlN and YSZ may be offset by the increased propensity to crack in LSC.

Figure 3.7 shows current measurements performed on undoped LC using the same scan conditions shown in Figure 3.5 for LSC. These graphs show a smaller leakage current of about 15 μA, consistent with the lower intrinsic conductivity of LC compared to LSC. At a laser power of 3 W (Figure 3.7 a), the current remains nearly constant when the laser is turned on and scans across the sample surface until a very small spike in current is detected close to when the laser reaches the negative electrode. This is a slightly smaller laser power required to initiate SLFS in LSC at this applied electric field. All the subsequent lines at increasing laser power exhibit small spikes in current near the completion of the scan, with increases in the magnitude of the current spike with increasing laser power. A maximum of almost 50 μA is observed for a laser power of 8 W, as shown in Figure 3.7 f). Compared to LSC, the magnitude of the spikes at a given laser power are much smaller, consistent with the earlier observations that the magnitude of the current spike is correlated to the initial leakage current.

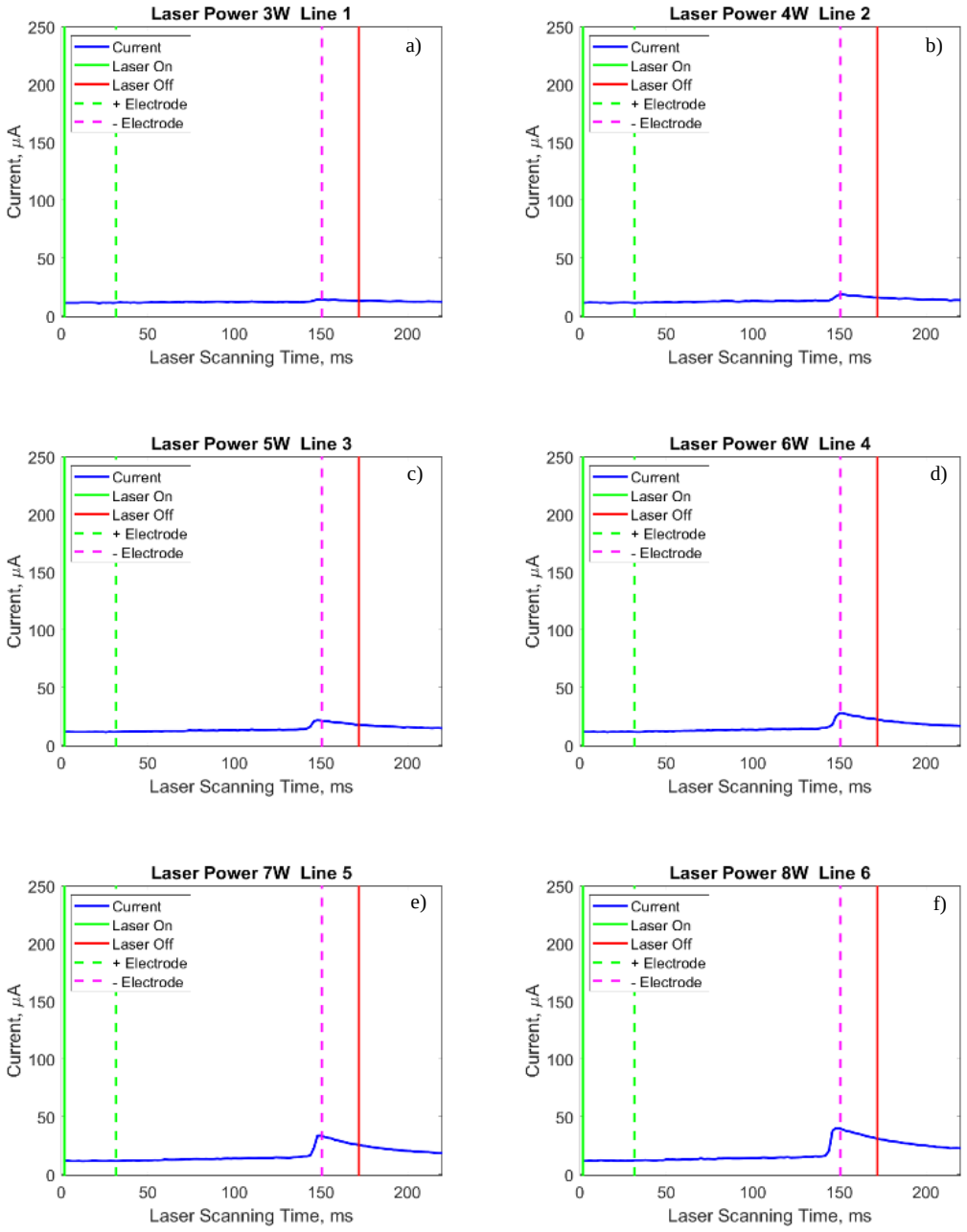

Figure 3.7. Influence of laser power on onset of SLFS in LC for a laser scan speed of 100 mm/s, applied electric field of 41 V/cm and laser power equal to a) 3W, b) 4W, c) 5W, d) 6W, e) 7W, and f) 8W.

An optical image of the pellet surface for LC is shown in Fig. 3.8 a). In contrast to the LSC pellet shown in Fig. 3.6, there are no visible tracks on the pellet surface where the laser power hits the sample, suggesting that the degree of sintering induced on the sample surface is much less in LC compared to LSC. Representative SEM images of the pellet surface in a region away from a scanned line (Fig. 3.8 b) and from the region near line 10 is shown in Figure 3.8 c). There do not appear to be significant differences in microstructure when comparing the unsintered pressed powder away from the scanned regions to the regions that were scanned, even at relatively large laser powers. This confirms that the visible indications of sintering like particle necking that were visible in LSC are much less prevalent in LC. This result is consistent with the observed much smaller current spikes observed for LC compared to LSC and suggest that there is a critical current of 50 - 75 μA required to induce significant changes in microstructure. Because the current never reaches 50 μA in LC this may explain why there were no observable changes in microstructure.

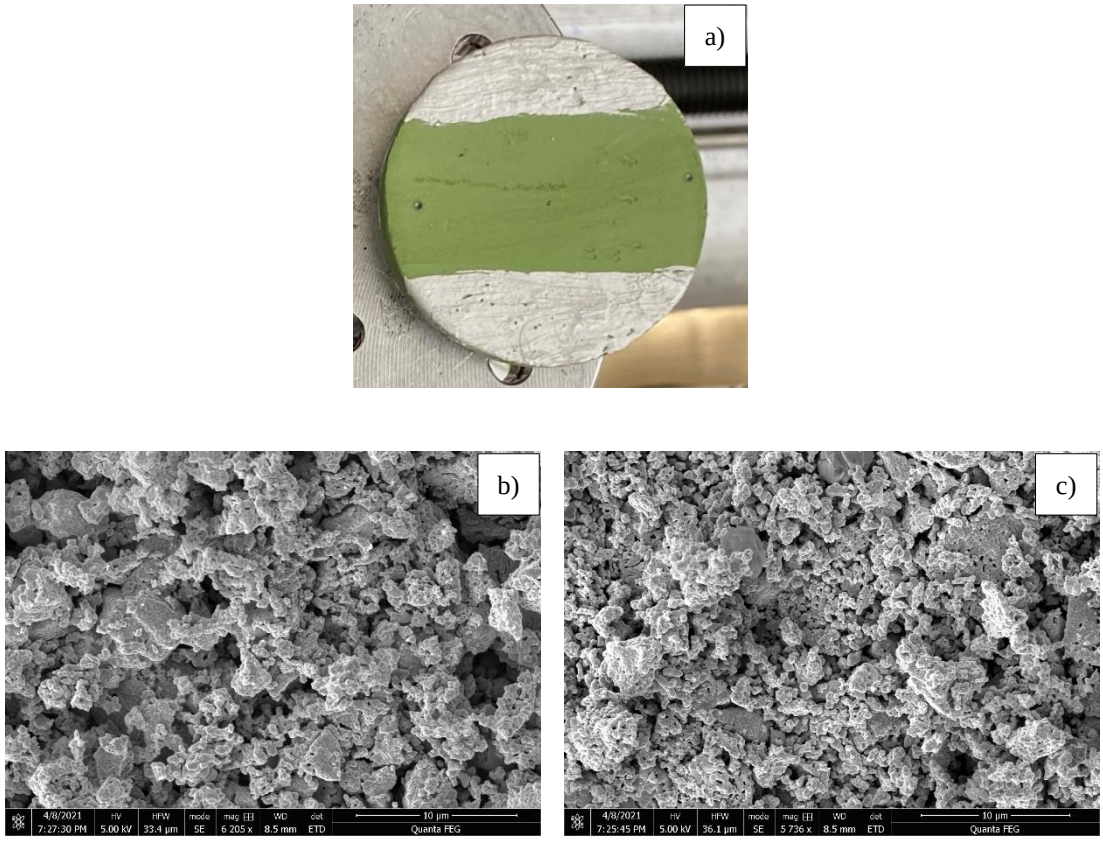

Figure 3.8. a) Picture of the pellet used for this study, and SEM images of. b) the pellet surface, and c) Region near line 10.

3.6. Study of Successive Scans for Doped and Undoped Lanthanum Chromite

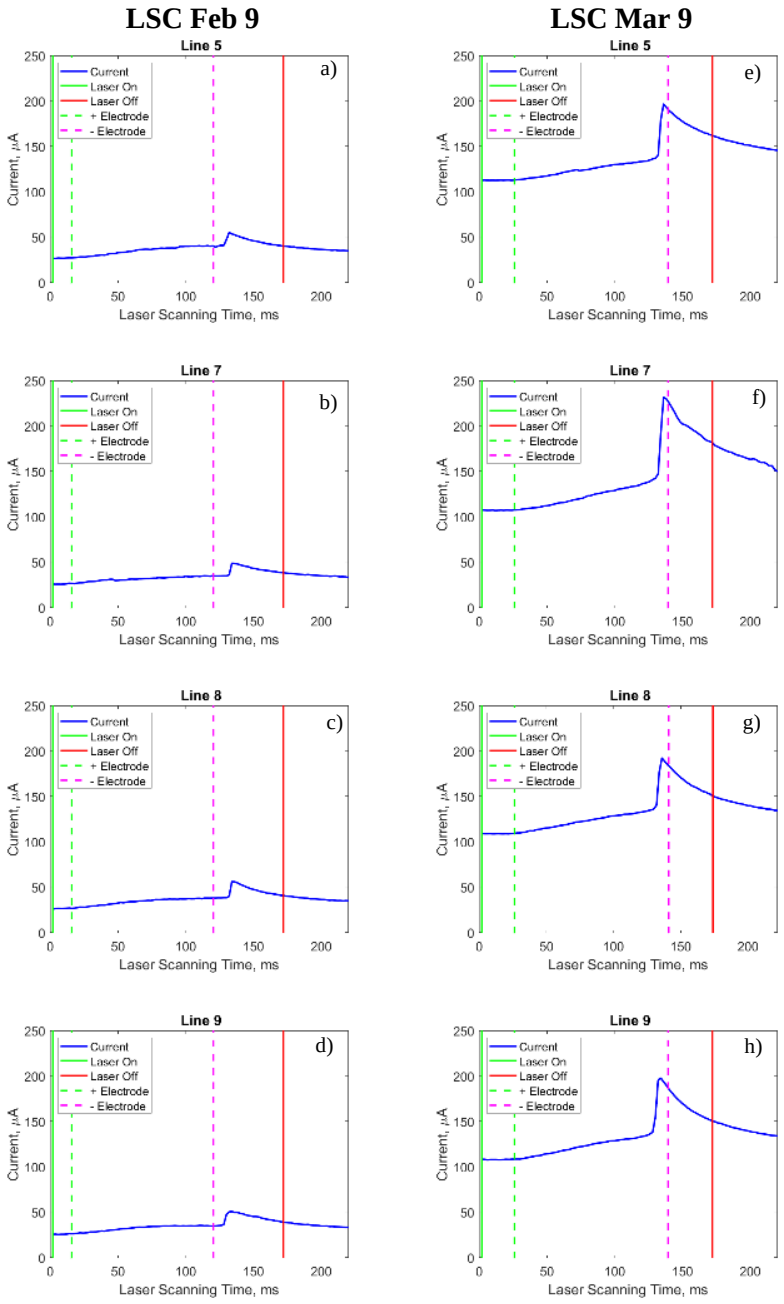

Figure 3.9.

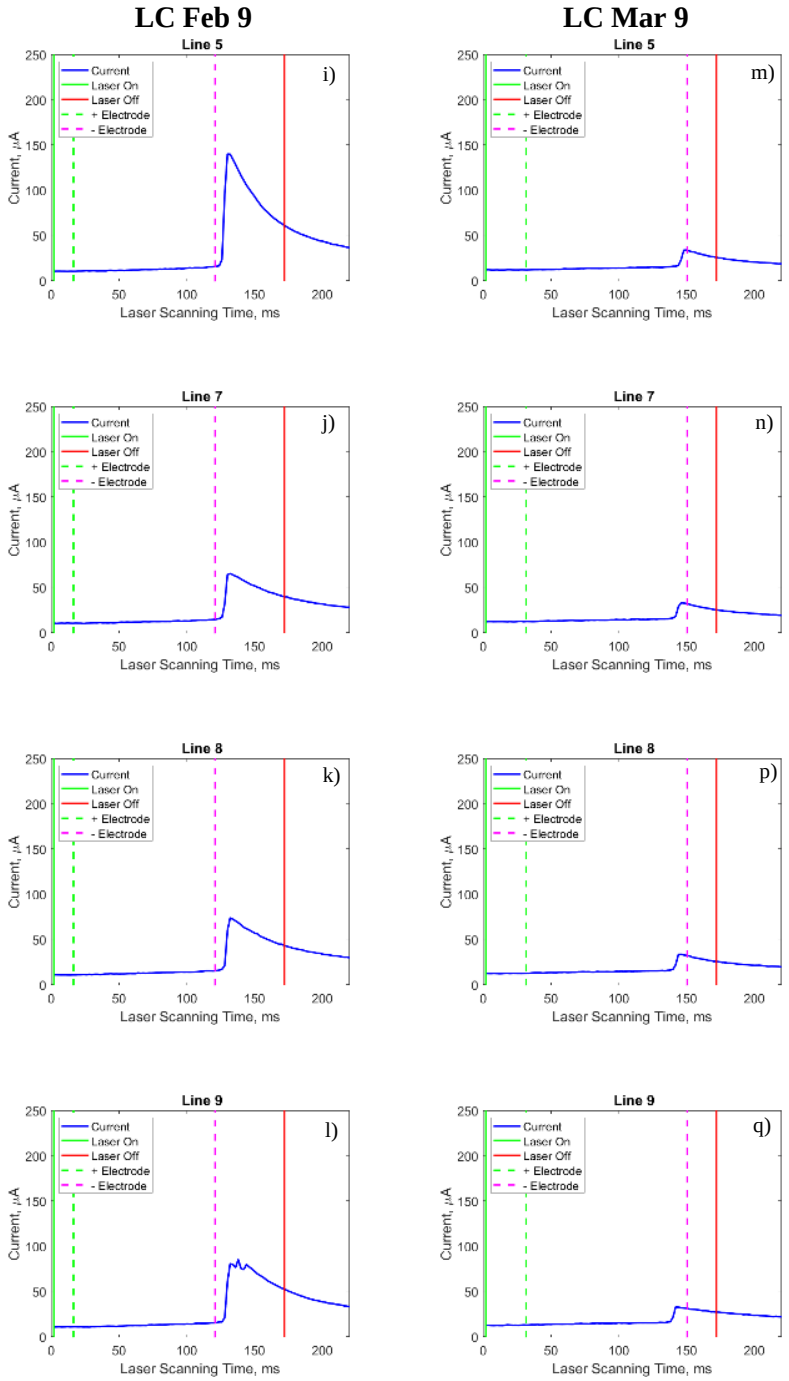
LC Feb 9
LC Mar 9
Line 5
Line 7
Line 8
Line 9
i)
j)
k)
l)
m)
n)
p)
q)
Current
Laser On
Laser Off
+ Electrode
- Electrode
Current, μA
Laser Scanning Time, ms

Figure 3.9.

Figure 3.9. Influence of successive scans on onset of SLFS. Columns 1 and 2 are for LSC, and Columns 3 and 4 are for LC. For each of these samples, lines 1 to 6 were scanned in succession with increasing laser power (data shown in previous sections) without cutting lines between each line scan. All the lines were cut after line 6 then line 7 and 8 were scanned subsequently, and then both lines (7 and 8) were cut before line 9 was scanned. All the lines presented here were performed at a laser power of 7 W, a scan speed of 100 mm/s scan speed, and an applied electric field of 41 V/cm.

Previous figures show that when SLFS initiates, current spikes which implies that there is some Joule heating along the line that may conduct heat to surrounding regions. If there is sufficient Joule heating from SLFS to change the microstructure far from the scanned line, one would expect that scanning a line might cause the response of subsequent parallel scans scanned with the same scan conditions and on the same pellet to show different responses. If the microstructure far from the scanned line is not affected by previous scans, there would not be an expected change for subsequent scan paths compared to the previous one. If scanning a line results in a sintered path that permanently increases the conductivity along that path there should be an increase in leakage current following a scan and this short circuit could produce additional Joule heating during subsequent line scans. The short circuit could then be removed by cutting the already scanned line.

This set of experiments were designed to study the influence of the previous lines on the behavior of the current for the subsequent lines while keeping all the parameters constant. Graphs of the current measurements of successive scan lines performed on LSC and LC samples with a laser power of 7 W, a scan speed of 100 mm/s and an applied electric field of 41 V/cm are shown in Figure 3.9. Two different pellets for each powder were used. Lines 1 to 6 were scanned at increasing laser power and the results reported in previous figures. After line 6 was scanned, all the lines were cut using a razor blade so that

these partially sintered regions could no longer conduct electricity, then line 7 and 8 were scanned subsequently, then both of them were cut before line 9 was scanned.

Figure 3.9. a) - d) shows current measurements for LSC_Feb_09. For this sample, a leakage current of approximately 25 µA is visible. In Figure 3.9.a) the current starts rising as the laser turns on and scans from the positive to the negative electrode and then it spikes by approximately 20 µA. For LSC_Mar_9 (Figure 3.9.e) - h)) the graphs show qualitatively similar behaviors to LSC_Feb_9, but with a much larger leakage current of approximately 110 µA and current spikes of approximately 100 µA except for line 7 (Figure 3.9. f)). This variations in leakage currents and current spikes for a given material from pellet-to-pellet has been described in Section 3.3 and is attributed to differences in particle packing and/or pressing defects.

For LC_Feb_9 (Figure 3.9. i) - l)) and LC_Mar_9 (Figure 3.9. m) - q)) the leakage current starts at a value of approximately 15 µA for both samples, the current remains nearly constant from the time the laser beam is turned on and scans across the pellet surface until the spike is detected for each line. The spikes in current vary from approximately 15 µA to more than 125 µA.

The results from this study show that there does not appear to be a systematic increase in peak current for subsequent scans scanned under the same scanning conditions that would suggest that SLFS in a line causes a change in microstructure far from the scanned line, for the scanning conditions used in this set of experiments.

These results also show that cutting the lines to remove the possibility of a short circuit also does not change the response for subsequently scanned lines. This confirms the assumption that a short circuit is not created for the conditions used in this set of experiments.

3.7. Study of Scan Pattern and Scan Direction on SLFS of Lanthanum Strontium Chromite

The value of the laser power for these experiments and the one reported in section 3.8 was interpolated from calibration data perform on January 30 of 2021 obtained with no chamber and thus with no ZnSe window, since the calibration obtained before for the laser power in the date of September 29 of 2020 was performed with the chamber on, and as mentioned before, all the experiments for this work were perform in air atmosphere and no additional chamber was used.

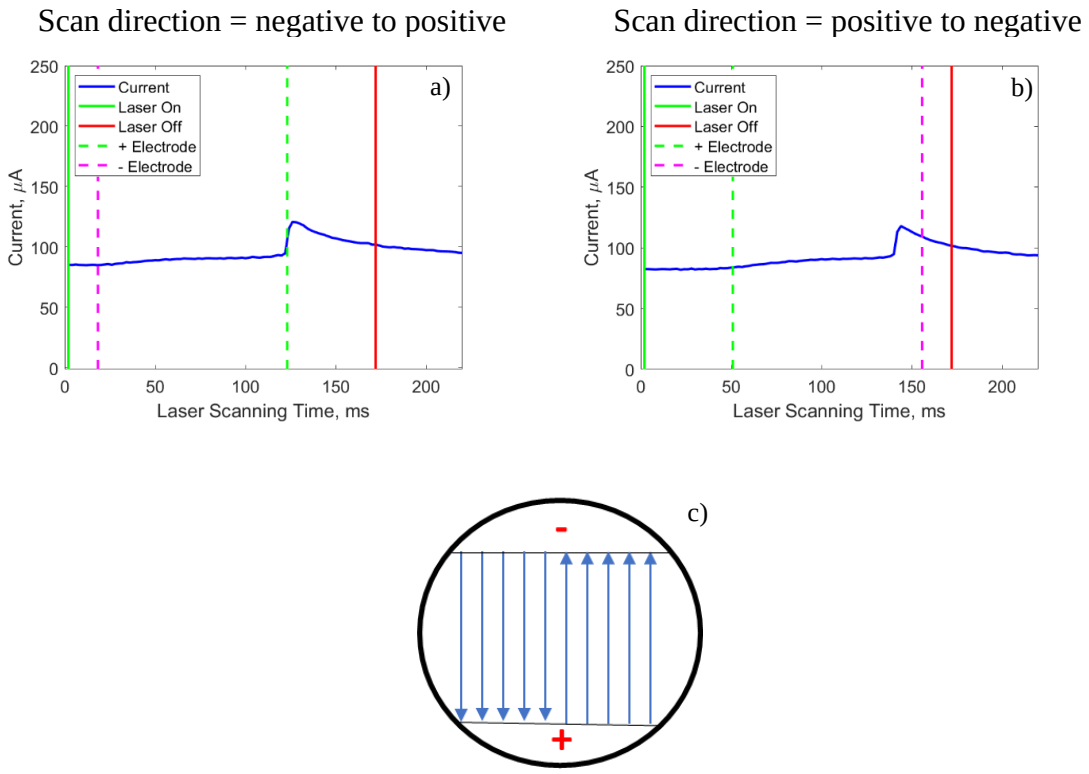

Figure 3.10. Influence of scan direction on the onset of SLFS for LSC at a laser power of 7 W, scan speed of 100 mm/s and an applied electric field equal to 19 V/cm. a) negative to positive and b) positive to negative. c) Shows the scan pattern that was used for this study.

Th influence of scan direction was studied using LSC pellets with an applied electric field of 19 V/cm, a scan speed of 100 mm/s and a laser power of 7 W. Multiple scan lines were repeated and representative currents measurements are shown in Figure 3.10 for the negative to positive direction (Fig. 3.10a) and the positive to negative direction (Fig. 3.10b).

The leakage current for this sample is of about 90 μA, under these experimental conditions. Both lines show a similar behavior that was previously explained. In this case the magnitude of the current spike is about 25 μA for both lines.

The responses were virtually identical for both lines which were ran in different directions. Keeping in mind that the current measurements are obtained only from the negative electrode, this suggests that the scanned regions are conductors. This can occur if the scanned regions remain hot at least until the laser reaches the opposite electrode from which the scanned commenced. Thus, the scanned regions are conducting paths because the high temperature increases the hole mobilities compared to the cold regions of the sample and allow holes to flow from the positive to the negative electrode. This scan pattern does not isolate the source of the holes. The source could be the positive electrode, or since the LSC is doped and contains a high concentration of holes, it could be the LSC powder itself.

3.8. STUDY OF PARTIAL SCANS ON LANTHANUM STRONTIUM CHROMITE

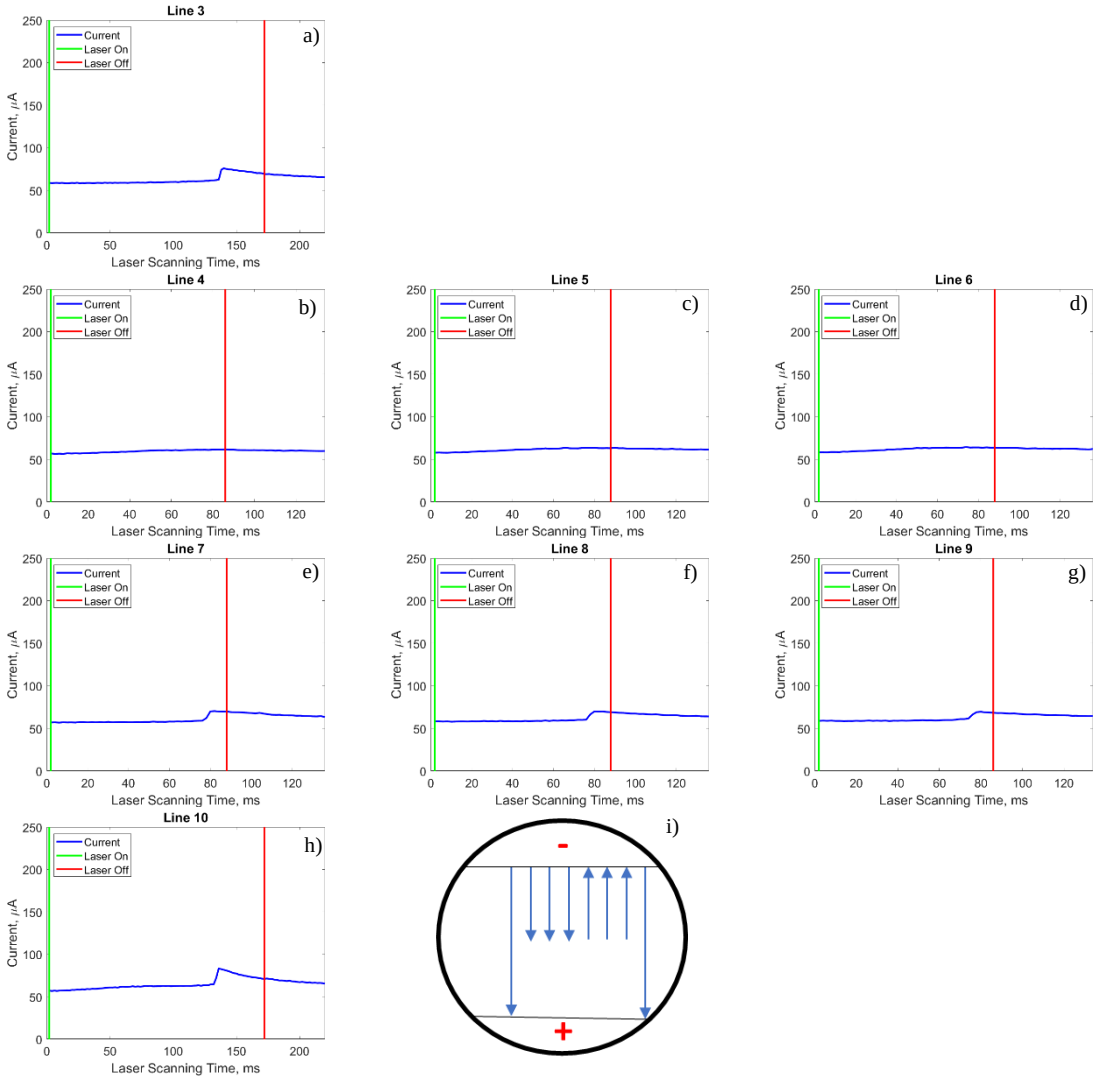

Figure 3.11. Influence of partial scans for LSC scanned at a laser power of 7 W, scan speed of 100 mm/s with an applied electric field of 16 V/cm, and with a scan pattern of a) full scan from negative to positive electrode, b), c) and d) partial scan originating at the negative electrode and scanned to near the center of the pellet, e), f) and g) partial scans originating near the center of the pellet and scanned to the negative electrode, h) full scan from negative to the positive electrode. Scan lines were cut after line 3, 6 and 9. i) Scan pattern used for this study.

A set of experiments was designed to determine the source of charge carrier during SLFS in LSC, which consisted of full and partial scans from the negative to positive electrode, and from the positive to the negative electrode as shown in Figure 3.11. Lines 1, 2 and 3 were scanned from the negative to the positive electrode and the graph of the current measurement for line 3 is shown in Figure 3.11. a). The lines were then cut and three partial scans (line 4, 5 and 6) were scanned from the negative electrode to approximately the center of the pellet (Figure 3.11 b), c) and d)). These three lines were cut and other three partial scans (line 7, 8 and 9) were scanned from approximately the center of the pellet to the negative electrode (Figure 3.11 e), f) and g)). Again, these three lines were cut and a full line (line 10) was scanned from the negative to the positive electrode and the graph of the corresponding current measurement is shown in Figure 3.11 h).

If the source of the carriers is only the metallic electrode, then SLFS would initiate only when we scan from one electrode to the other. In this case the scanned region would provide a conducting path from electrode to electrode. If extrinsic holes from doping are activated by heating the scanned line regions, SLFS could be initiated with partial scans from or to the negative electrode with similar responses in scanning in either direction. If intrinsic holes are generated within the ceramic during scanning by heating, we would expect for SLFS to initiate even from partial scans, but there could be different responses depending on the scan direction.

Lines 3 and 10 show a similar behavior that has previously been described, with a leakage current of approximately 60 μA, and a spike of approximately 20 μA for both lines. Lines 4 to 6 show a different behavior than what was previously observed. In these lines a buildup of charge is observed, but no current spike is detected in any of the lines. Lines 7 to 9 do show a spike in current of about 10 μA as the laser approaches the negative electrode

and the laser is turned off, which is smaller than what was measured from the full line scan from negative to positive electrode.

From the results obtained in this study it is apparent that intrinsic holes may be concentrated in the region directly under the laser since this is the hottest region. Scanning from the negative electrode towards the center of the sample (lines 4 to 6) does not produce a significant current because the holes are pulled by the scanning laser towards the center of the sample, where they are trapped, so no significant change in current can be measured. In this case a small number of holes are able to make it back to the negative electrode by conducting along the cooling line to produce a very small current rise. In lines 7 to 9 the carriers follow the scanning laser until it reaches the negative electrode, and the holes produce a current spike.

In summary, these results show that electronic carriers are responsible for SLFS in LC and LSC. Doping LC with strontium to produce LSC results in a larger fraction of extrinsic electronic carriers which increases the concentration of room temperature carriers that are responsible for the increased leakage currents measured in LSC compared to LC. The increased temperatures that arise during laser scanning increase the carrier mobilities and also increase the concentration of intrinsic carriers. Our results show that the carrier concentration and mobilities are strongly affected by the local hot region directly under the laser beam.

Chapter 4: Conclusions and Future Work

4.1. Conclusions

The primary objective of this work was to study the effects that varying the electrical conductivity of ceramics has on the onset of SLFS. To do this, two materials were studied: pure lanthanum chromite (LC) and doped lanthanum strontium chromite (LSC).

Relative to previous ceramics that have been used to study SLFS that have poor electrical conduction (YSZ and AlN), pure LC is an intrinsic electronic conductor with excellent conductivity. The induced extrinsic charge carrier concentration resulting from doping LC with strontium to produce LSC further increases its electronic conductivity. This is directly observable from the room-temperature leakage current measured when an electric field is applied to samples of LC and LSC. Significantly higher leakage currents were measured in LSC than LC and both exhibited much higher leakage currents compared to previously studied AlN and YSZ.

Measurements of current versus laser scan time were used to assess the onset of SLFS. It was observed that there was a minimum electric field required to initiate SLFS of 41 V/cm for LC and of 16 - 41 V/cm for LSC. These values of applied electric field required to initiate SLFS in LC and LSC are two orders of magnitude lower than what was previously observed for YSZ and AlN, which confirms that the initiation of SLFS is easier for ceramics that have high electrical conductivity such as LC and LSC.

Critical laser power for SLFS initiation on LC and LSC under an applied electric field of 41 V/cm was shown to be 4 W and 3 W, respectively. The unexpected lower laser power required to initiate SLFS in LC could be due to more conductive paths present in the powder due to the reduced size of the powder agglomerates and the resulting higher green density that was observed for the LC powder compared to the LSC powder.

For LSC, the magnitude of the peak current measured during the onset of SLFS for an applied electric field of 41 V/cm increased with increasing laser power up to a laser power of 5 W. Further increases in laser power did not show the expected monotonic increase in peak current. SEM images revealed the presence of cracks in the samples after SLFS that likely resulted from thermal shock that occurred during SLFS. Increasing severity of cracking with laser power may explain the non-monotonic peak current response. The presence of cracks would be expected to interfere with the conduction of current through the ceramic part, but larger laser powers also result in a larger volume of hot material that is more highly conductive. The measured peak current therefore would be expected to depend on the probability of accessing a continuous, crack-free, hot path from one electrode to the other, which would explain the observed non-monotonic behavior.

For the LC material, the magnitude of the peak current did increase monotonically with increasing laser power. This is expected since the higher laser power results in higher sample temperatures and thus a higher concentration of temperature-activated intrinsic charge carriers that have higher mobility. Unlike the LSC, SEM images of the microstructure did not show evidence of partial sintering close to the regions where the lines were scanned. This is consistent with the much smaller peak currents (< 50 μA) measured in LC compared to LSC (> 50 μA) and it suggests that a minimum peak current of ≈ 50 μA is required to observe changes in powder morphology in these materials.

Performing successive parallel scans on the same pellets of LC and LSC with the same scanning conditions does not appear to result in a change in current response. This suggests that the permanent increase in conductivity that results from scanning a line (a short circuit) does not result in significant Joule heating during scanning of the successive lines. Removing previous scanned lines before scanning successive lines to remove the possibility of a short circuit also does not show a significant effect on the measured current

when SLFS occurs. This confirms that no significant changes in microstructure occur far from the scanned line and that there is no significant history effect on successive lines scanned on the same pellets.

No significant differences in the current measurements were observed with scanning direction when scanning from the positive to the negative electrode versus scanning from the negative to the positive electrode. Since current in these experiments was only measured at the negative electrode, this does not reveal information about the symmetry or asymmetry of flux for electrons and holes responsible for the current. It does however suggest that cooling that takes place behind the scanning laser beam is not significant during the time it takes to scan across the sample surface because scan direction does not influence the flux of holes that arrive at the negative electrode during SLFS.

A partial scan study was designed to determine the source of the charge carriers during SLFS of LSC. SLFS was observed to initiate from partial scans that started from near the middle of the pellet and were scanned to the negative electrode. However, SLFS was not observed to initiate when partial scans were started on the negative electrode and scanned to a spot near the middle of the pellet. This suggests that activated charge carriers may follow the hot region under the scanning laser to the negative electrode where the current measurement is obtained.

Comparing the current measured during the partial scans and full scan lines, the full scan lines show higher measured current than equivalent partial scan lines performed at the same laser power and applied electric field. This is consistent with the assumption that a combination of electrons coming from the positive electrode, intrinsic charger carriers activated due to heating with the laser, and the extrinsic charge carriers present in LSC due to doping are responsible for the current measured in a full scanned line during SLFS of LSC.

4.2. SUGGESTED FUTURE WORK

The following are suggested future work.

- Perform quantitative electrical conductivity measurements of the samples. Since impurities were found in the XRD analysis in LSC, this could have a significant effect on conductivity of this material compared to previously reported conductivities for LSC from the literature.
- Run the experiments for LC at lower applied electric field to identify the minimum applied electric field required to initiate SLFS in this material. This would require that a different power supply be used since the one employed for the experiments used in this study was not stable below 41 V/cm.
- Perform more SEM analysis of the cracks formed on LSC during increasing laser power studies to determine if there is a correlation between the severity of the cracks (spatial density of cracks and depth of the cracks into the sample) and the laser power.
- Perform the same partial scan and scan direction experiments on LC that were performed on LSC. This would allow us to determine if the concentration of activated intrinsic charge carriers due to heating with the laser is sufficient to initiate SLFS in this material. Further studies at higher applied electric fields and higher laser power for these experiments might be necessary.
- Perform SEM analysis of the partial scans that initiated SLFS to verify the degree of sintering obtained and if cracks were formed in these lines.

- Perform SEM analysis of the partial scanned lines that did not initiate SLFS to verify if sintering of the lines occurred even though spikes in current that we use to identify the onset of SLFS were not observed.
- Perform simulations of SLFS on LSC and LC to predict their behavior under the experimental conditions of this process based on their physical properties. Additional materials properties measurements might be necessary to perform these simulations.

References

[1] M. N. Rahaman, *Ceramic processing and sintering*, Second Edi. Boca Raton: CRC Press, 2003.

[2] Bourell; D.L.; Beaman; J.J.; Marcus; H.L.; Barlow; J.W., *Solid Freefor Fabrication: An Advanced Manufacturing Approach*. 1990, pp. 1–7.

[3] ISO/ASTM, "Additive Manufacturing - General Principles Terminology (ASTM52900)," *Rapid Manuf. Assoc.*, pp. 10–12, 2013, doi: 10.1520/F2792-12A.2.

[4] C. Barry Carter and M. Grant Norton, *Ceramic materials: Science and engineering*. 2007.

[5] Richerson David W., *Modern Ceramic Engineering:Properties, Processing, and use in Design*. 2006.

[6] M. Cologna, B. Rashkova, and R. Raj, "Flash sintering of nanograin zirconia in <5 s at 850°C," *J. Am. Ceram. Soc.*, vol. 93, no. 11, pp. 3556–3559, 2010, doi: 10.1111/j.1551-2916.2010.04089.x.

[7] H. Yoshida, Y. Sakka, T. Yamamoto, J. M. Lebrun, and R. Raj, "Densification behaviour and microstructural development in undoped yttria prepared by flash-sintering," *J. Eur. Ceram. Soc.*, vol. 34, no. 4, pp. 991–1000, 2014, doi: 10.1016/j.jeurceramsoc.2013.10.031.

[8] M. Cologna, J. S. C. Francis, and R. Raj, "Field assisted and flash sintering of alumina and its relationship to conductivity and MgO-doping," *J. Eur. Ceram. Soc.*, vol. 31, no. 15, pp. 2827–2837, 2011, doi: 10.1016/j.jeurceramsoc.2011.07.004.

[9] J. S. C. Francis and R. Raj, "Influence of the field and the current limit on flash sintering at isothermal furnace temperatures," *J. Am. Ceram. Soc.*, vol. 96, no. 9, pp. 2754–2758, 2013, doi: 10.1111/jace.12472.

[10] D. Hagen, J. J. Beaman, and D. Kovar, *Onset of Selective Lasre Flash Sintering in 8YSZ*. 2020.

[11] S. K. Jha, K. Terauds, J.-M. Lebrun, and R. Raj, "Beyond flash sintering in 3 mol % yttria stabilized zirconia," *J. Ceram. Soc. Japan*, vol. 124, no. 4, pp. 283–288, 2016, doi: 10.2109/jcersj2.15248.

[12] D. Yang and H. Conrad, "Enhanced sintering rate of zirconia (3Y-TZP) by application of a small AC electric field," *Scr. Mater.*, vol. 63, no. 3, pp. 328–331, 2010, doi: 10.1016/j.scriptamat.2010.04.030.

[13] J. S. C. Francis, M. Cologna, and R. Raj, "Particle size effects in flash sintering," *J. Eur. Ceram. Soc.*, vol. 32, no. 12, pp. 3129–3136, 2012, doi: 10.1016/j.jeurceramsoc.2012.04.028.

[14] M. Cologna, A. L. G. Prette, and R. Raj, "Flash-sintering of cubic yttria-stabilized zirconia at 750°C for possible use in SOFC manufacturing," *J. Am. Ceram. Soc.*, vol. 94, no. 2, pp. 316–319, 2011, doi: 10.1111/j.1551-2916.2010.04267.x.

[15] R. Baraki, S. Schwarz, and O. Guillon, "Effect of electrical field/current on sintering of fully stabilized zirconia," *J. Am. Ceram. Soc.*, vol. 95, no. 1, pp. 75–

78, 2012, doi: 10.1111/j.1551-2916.2011.04980.x.
[16] R. Raj, “Joule heating during flash-sintering,” *J. Eur. Ceram. Soc.*, vol. 32, no. 10, pp. 2293–2301, 2012, doi: 10.1016/j.jeurceramsoc.2012.02.030.
[17] A. L. G. Prette, M. Cologna, V. Sglavo, and R. Raj, “Flash-sintering of Co2MnO4 spinel for solid oxide fuel cell applications,” *J. Power Sources*, vol. 196, no. 4, pp. 2061–2065, 2011, doi: 10.1016/j.jpowsour.2010.10.036.
[18] A. Uehashi, H. Yoshida, T. Tokunaga, K. Sasaki, and T. Yamamoto, “Enhancement of sintering rates in BaTiO3 by controlling of DC electric current,” *J. Ceram. Soc. Japan*, vol. 123, no. 1438, pp. 465–468, 2015, doi: 10.2109/jcersj2.123.465.
[19] A. Gaur and V. M. Sglavo, “Densification of La0.6Sr0.4Co0.2Fe 0.8O3 ceramic by flash sintering at temperature less than 100 °c,” *J. Mater. Sci.*, vol. 49, no. 18, pp. 6321–6332, 2014, doi: 10.1007/s10853-014-8357-2.
[20] H. Yoshida, P. Biswas, R. Johnson, and M. K. Mohan, “Flash-sintering of magnesium aluminate spinel (MgAl2O4) ceramics,” *J. Am. Ceram. Soc.*, vol. 100, no. 2, pp. 554–562, 2017, doi: 10.1111/jace.14616.
[21] R. Muccillo and E. N. S. Muccillo, “Electric field assisted sintering of electroceramics and in situ analysis by impedance spectroscopy,” *J. Electroceramics*, vol. 38, no. 1, pp. 24–42, 2017, doi: 10.1007/s10832-016-0054-x.
[22] “2016_Yaxi_Estimating Joule heating and ionic conductivity during flash sintering of 8YSZ _ Elsevier Enhanced Reader.pdf.” .
[23] J. Beaman, D. Kovar, D. Bourell, and D. Hagen, “Systems and methods for additive manufacturing of ceramics,” 2018.
[24] D. Hagen, D. Kovar, and J. J. Beaman, “Effects of Electric Field on Selective Laser Sintering of Yttria-Stabilized Zirconia Ceramic Powder,” pp. 909–913, 2018.
[25] D. Hagen, A. Chen, J. J. Beaman, and D. Kovar, “Moisture effects on selective laser flash sintering of yttria-stabilized zirconia,” *Solid Free. Fabr. 2019 Proc. 30th Annu. Int. Solid Free. Fabr. Symp. - An Addit. Manuf. Conf. SFF 2019*, pp. 873–891, 2019.
[26] D. Hagen, J. J. Beaman, and D. Kovar, “Selective laser flash sintering of 8-YSZ,” *J. Am. Ceram. Soc.*, vol. 103, no. 2, pp. 800–808, 2020, doi: 10.1111/jace.16771.
[27] A. Gouws, J. Beaman, and D. Kovar, *Initial Stage Selective Laser Flash Sintering of Aluminum Nitride*. 2020.
[28] D. B. Meadowcroft, “Some properties of strontium-doped lanthanum chromite,” *J. Phys. D. Appl. Phys.*, vol. 2, no. 9, pp. 1225–1233, 1969, doi: 10.1088/0022-3727/2/9/304.
[29] T. Ishikawa, *Perovskite Oxide for Solid Oxide Fuel Cells*. Dordrecht: Springer, 2009.
[30] P. Sujatha Devi and M. Subba Rao, “Preparation, structure, and properties of strontium-doped lanthanum chromites: La1-xSrxCrO3,” *J. Solid State Chem.*, vol. 98, no. 2, pp. 237–244, 1992, doi: 10.1016/S0022-4596(05)80231-2.

[31] A. Gouws, D. Hagen, A. Chen, E. Kardoulaki, J. J. Beaman, and D. Kovar, "Selective Laser Flash Sintering of AlN," *Int. J. Appl. Ceram. Technol.*, p. 2020, 2020.
[32] A. Chen, J. Beaman, and D. Kovar, *Local Temperature Distributions during Selective Laser Flash Sintering*. 2020.